Research papers

Effects of vegetation density on flow, mass exchange and sediment transport in lateral cavities

Luiz E.D. de Oliveira [a,b,*], Taís N. Yamasaki [a,c], Johannes G. Janzen [a], Carlo Gualtieri [b]

[a] Faculty of Engineering, Architecture and Urban Planning, and Geography, Federal University of Mato Grosso do Sul, Campo Grande, Brazil
[b] University of Napoli "Federico II", Napoli, Italy
[c] Department of Geography, Durham University, Durham, UK

ARTICLE INFO

ABSTRACT

Large-Eddy Simulations (LES) were used to investigate the hydrodynamics and mass transfer between the flow in the main channel and a vegetated lateral cavity. Fourteen vegetation densities (0 to 10.65 %) were tested, revealing two distinct hydrodynamic patterns. For cavities with low vegetation density ($a < 3.99$ %), one primary gyre in contact with the interface between main channel and cavity with high velocity was formed; the thickness of the mixing layer grew longitudinally along the interface, and regions with high vorticity and turbulence kinetic energy appeared at the interface and inside the cavity. For cavities with high vegetation density ($a > 3.99$ %), two gyres in contact with the interface with low velocity were formed, the thickness of the mixing layer did not grow, and the vorticity and turbulence kinetic energy were low inside the cavity. The mass transport presented the same threshold value as the hydrodynamics ($a = 3.99$ %). For cavities with low vegetation density, a fast mass transfer occurred through the interface between the main channel and cavity and inside the cavity, while the opposite was observed for cavities with high vegetation density. Finally, the modelled hydrodynamics was used to infer possible sediment deposition patterns and flow resistance.

1. Introduction

Lateral cavities are an important component of channel systems (Harvey and Gooseff, 2015) because they (i) act as a macro-roughness at the riverbanks (Juez et al., 2018a), (ii) act as transient storage zones (Drost et al., 2014; Jackson et al., 2015, 2013), and (iii) enhance biodiversity in the system (Harvey, 2016; Ribi et al., 2014; Watts and Johnson, 2004; de Oliveira et al., 2023a). In relation to (i) and (ii), many anthropogenic actions and natural events (e.g., hydropeaking) might cause rapidly varied unsteady flow in channels, and measures such as lateral cavities at the banks can increase their flow resistance and natural retention capacity (Meile et al., 2010). With respect to (ii), lateral cavities are major storage regions for pollutants, nutrients, gases, and sediments, since this material is transported towards the cavity from the main channel, and the flow velocities are lower than the main channel within the cavities. Finally, in relation to (iii), cavities create flow velocity and morphology diversity, promoting the development of habitats within a channel with require areas with heterogeneity.

The lateral cavities of open-channel flows can be divided into two types: the so-called "lateral cavity" (Fig. 1) and the "cavity between two groynes" (Mignot et al., 2019). In the lateral cavity, the flow reaching the upstream corner is parallel to the interface of the main channel and the cavity, while in a cavity between two groynes the incoming flow is slightly directed away from the interface of the main channel and the cavity towards the centre of the main channel. These two types of cavities can either be spaced at sufficient streamwise distances along a channel, such that the upstream flow is unaffected by any upstream mixing layer (e.g., Xiang et al., 2019), or built-in series, and the mixing layer grows downstream from the leading edge of the first cavity and then stabilizes (reaching a fully developed state) by the fourth to sixth cavity (e.g., McCoy et al., 2007). The focus of this study was on isolated lateral cavities, which can be formed naturally (e.g., natural irregularities of the banks) or by human intervention (e.g., canals) (Engelen et al., 2021).

Mignot et al. (2019) showed that the aspect ratio W/L (where W is the cavity width and L is its length) divides the flow inside cavities into

four categories: (i) for $0.2 < W/L < 0.33$, the cavity is dominated by a highly distorted single vertical axis recirculation; (ii) for $0.3 < W/L < 0.6$, two contra-rotating recirculations are aligned along the channel axis: a recirculation occupying most of the cavity and a small recirculation located in the upstream corner; (iii) for $0.6 < W/L < 2$, a single recirculation, approximately circular, occupies the whole cavity; (iv) for $2 < W/L < 3$, two contra-rotating recirculations are aligned perpendicularly to the interface.

Despite the horizontal dimensions of the recirculating flow, in the cavity, are typically significantly greater than the water depth, the flow is three-dimensional (Tuna et al., 2013). For example, the cavity-main channel interface is mainly characterised by the vortex shredding and its velocity variation in the depth axis (Engelen et al., 2020). The fluid enters the cavity primarily through the bottom layer of the downstream interface and exits primarily through the top layer of the upstream interface (Xiang et al., 2020). This feature is related to the velocity difference between the main channel and the cavity, which forms a mixing layer at the interface that exhibits shear instability. Shedding vortices form at the cavity's upstream edge, and the mixing layer carries them downstream. Some of these vortices are injected into the cavity in the form of a wall-attached jet-like flow that is parallel to the downstream wall. This mixing layer, with its vortices, controls the exchange of mass between the main channel and the cavity (Constantinescu et al., 2009).

The investigation of momentum and mass transport along the interface between a cavity and the main channel poses challenges for experimental analysis. Numerous studies have operated under the assumption that mass exchange between these two domains is primarily governed by transverse velocity components across the interface, lending itself to parameterization by a singular exchange velocity. This convention often presumes a two-dimensional flow and designates the exchange velocity either at the free surface, as observed through surface particle tracking, or at a depth deemed representative of the depth-averaged flow field, employing methods such as sub-surface particle image velocimetry (Engelen et al., 2021). However, it should be noted that this generalization does not hold true, particularly at the intricate interface.

Recent work by Engelen and De Mulder (2020) and subsequently by Engelen et al. (2021) has employed Particle Tracking Velocimetry (PTV) to assess the three-dimensional flow characteristics and mass exchange at the interface between a cavity and the main channel. Their findings have revealed that the transverse velocity approach tends to overestimate the extent of interfacial mass exchange.

An alternative method for determining interfacial mass exchange involves the utilization of the tracer release method. In this technique, a passive tracer is instantaneously introduced into the cavity, with the reduction in volume-averaged concentration tracked as the tracer is washed out into the main channel. Notably, laboratory or field experiments reliant on volume-averaged concentration measurements confront substantial challenges and inherent uncertainties (Altai and Chu, 1997; Booij, 1989; Kozerski et al., 2006; Kurzke et al., 2002; Mignot et al., 2017; Sanjou and Nezu, 2013; Weitbrecht et al., 2008). The intricacy lies in the uniform injection of tracer throughout the lateral cavity in an instantaneous manner, coupled with the fact that the measurement represents not a genuine volumetrically averaged concentration, but rather an approximation confined to a segment of the cavity volume (Mignot et al., 2017).

To address these experimental challenges and gain a deeper insight into the intricacies of processes within channel flow cavities, numerical simulations have been employed. Reynolds-averaged Navier–Stokes (RANS) simulations have been extensively used due to their computational efficiency and ability to replicate observed flow patterns within the cavity. However, RANS simulations fall short in accurately capturing the momentum and mass exchange occurring across the interface that separates the main channel from the cavity (Gualtieri et al., 2010). In response to these limitations, Large Eddy Simulation (LES) has gained increasing popularity. Unlike RANS, LES offers the advantage of higher accuracy in flows dominated by shear-layer vortices, a characteristic feature of the interface between the main channel and the cavity (Xiang et al., 2019). LES also provides comprehensive insights into turbulent flow dynamics, which are fundamentally responsible for governing mass and momentum exchange processes (Constantinescu et al., 2009; Lu and Dai, 2016; Ouro et al., 2018). Additionally, LES is increasingly being recognized as a viable alternative to the prevailing industrial practice, which predominantly relies on RANS approaches (Zhiyin, 2015).

Numerical simulations and experimental investigations have been extended to encompass vegetated cavities as well. Vegetation is known to create a conducive environment for retaining fine sediments and nutrients (Asaeda et al., 2009; Barko et al., 1991; Cotton et al., 2006; Ely and Evans, 2010; Jones, 2020; Nepf, 2012a; Olesen, 1996; Vandenbruwaene et al., 2011; Ward et al., 1984). Once established, vegetation engenders a diversity of ecosystem services, encompassing the provision of shelter for aquatic communities (Arend and Bain, 2008; Kraus and Jones, 2012; Maceina et al., 1999), the entrapment of suspended materials (Ward et al., 1984), safeguarding against erosion (Duró et al., 2020), enhancing water quality (Zhang et al., 2021), facilitating carbon storage (Engelhardt et al., 2004; Zhang et al., 2021), and nurturing an expansive array of infauna (Buczyński et al., 2017; Engelhardt et al., 2004; Staentzel et al., 2019; Zhang et al., 2021). A significant portion of these services emanates from the modifications in flow dynamics
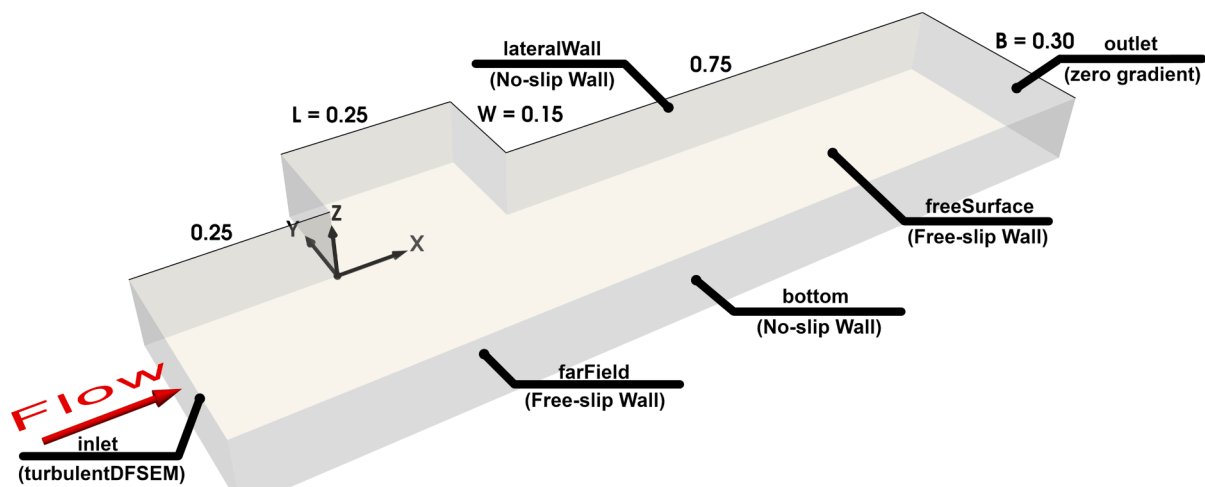

Fig. 1. Computational domain with coordinates, sizes and main boundary conditions. All the sizes are in metres.

wrought by the presence of vegetation within cavities.

For instance, the introduction of vegetation can reduce flow velocity and turbulence, thereby fostering sedimentation and curtailing the initiation and resuspension of sediment motion. This effect translates into augmented light penetration, heightened oxygen concentration, and consequently, an enhancement of vegetation growth (Brodersen et al., 2017; Watanabe et al., 2002). Furthermore, through the attenuation of bed-shear stress, vegetation affords protection to the substrate and roots, thereby bolstering soil stability against erosion and creating an environment conducive to the establishment and endurance of new vegetation (Vargas-Luna et al., 2015). Thus, a comprehensive understanding of the ecosystem services furnished by cavities necessitates the thorough investigation of hydrodynamic alterations stemming from the presence of vegetation.

The influence of vegetation on hydrodynamics within cavities is characterized by complexity, given its reliance on the attributes of the vegetation itself, as well as the distinctive features of the main channel and the cavity (Lu and Dai, 2016; Sukhodolov et al., 2017; Xiang et al., 2020, 2019). Notably, vegetation density possesses a dual role in effecting alterations: on one hand, it can engender a reduction in flow velocity and turbulence, thereby molding the circulation patterns within the cavity. A case in point is the transformation noted by Sukhodolov et al. (2017), who reported a shift from the conventional twin counter-rotating circulation pattern to a singular circulation pattern characterized by augmented vegetation density. In contrast, studies by Lu and Dai (2016) and Xiang et al. (2019) have indicated that analogous circulation patterns can still persist within cavities, irrespective of the presence or absence of vegetation and its density. Thus, a unanimous consensus remains elusive regarding the implications of vegetation for the flow patterns within cavities. Furthermore, Sukhodolov et al. (2017) observed that emergent vegetation within the cavity yielded marginal impact on the dynamics of the mixing layer at the interface between the main channel and the cavity. Conversely, Xiang et al. (2020) demonstrated a distinct connection between vegetation density and interface flow. To illustrate, Xiang et al. (2020) appointed that an augmented density of vegetation within the cavity resulted in a diminished inner thickness of the mixing layer separating the main channel and the cavity. This diminution was attributed to the heightened obstruction effect exerted by the vegetation, impeding the infiltration of the mixing layer and thereby restricting its expansion. Notably, the outer mixing layer remained nearly unaffected by the presence of vegetation within the cavity (Xiang et al., 2020). Crucially, the dynamics of the mixing layer bear direct consequences on mass exchange between the main channel and the cavity. This stems from the fact that the mixing layer orchestrates the detachment of vortices and the ensuing momentum exchange (Xiang et al., 2020).

The existing body of research furnishes an overarching portrayal of flow characteristics within vegetated cavities, yet certain aspects warrant further exploration. For instance, preceding investigations have scrutinized vegetation density (a) across the range of 0 to 1.57 % (Sukhodolov et al., 2017; Xiang et al., 2019, 2020). Nevertheless, a definitive threshold demarcating "dense" or "sparse" vegetation in cavities, contingent upon flow characteristics, remains elusive. For emergent vegetation patches in an open channel, for example, Chen et al. (2012) characterized the vegetation as being "dense" or "sparse" according to flow blockage thresholds, in which the flow properties near the patch (e.g., flow adjustment length and the velocity exiting the patch) were distinct above and below the threshold. A similar approach can be done for vegetated cavities for a wider range of vegetation density found in the literature. The vegetation density of vegetated channels varies between 0.7 and 51 % (Chen et al., 2012). Further, past investigations into the dynamics of mass transport within vegetated cavities have largely relied on velocity field analysis. However, this approach remains insufficient in encapsulating the entirety of the exchange process (Engelen et al., 2021). Therefore, a more expansive exploration of mass exchange through tracer injection, as advocated by

Xiang et al. (2019), is warranted. Additionally, no other study inferred the dynamics of sediment transport in vegetated lateral cavities, and how the change in vegetation density affects its features.

The current study is hence designed with the objective of extending the range of tested vegetation densities within cavities. Furthermore, it seeks to elucidate potential thresholds governing hydrodynamics and mass exchange processes. To achieve these objectives, the study employs Large Eddy Simulation (LES) to simulate both hydrodynamics and the interfacial mass exchange. The simulation also offers insights into sediment transport.

2. Numerical model

2.1. Model equations

The simulations were performed with the Large Eddy Simulation (LES) approach, which uses the spatial filtering of the incompressible Navier-Stokes equations to solve for the fluid motion and turbulence (Rodi et al., 2013). For an incompressible fluid, the conservation equations of mass and momentum are, respectively:

$$\frac{\partial \overline{u_i}}{\partial x_i} = 0 \tag{1}$$

$$\frac{\partial \overline{u_i}}{\partial t} + \frac{\partial}{\partial x_j}\left(\overline{u_i u_j}\right) = \frac{-1}{\rho}\frac{\partial \overline{p}}{\partial x_i} + \frac{\partial}{\partial x_j}\left[\vartheta\left(2\overline{S_{ij}}\right) - \tau_{ij}\right] + \overline{S}_{M,i} \tag{2}$$

in which the overbar indicates resolved quantities, and i and j = 1, 2, 3 correspond to x, y, z directions, respectively; u_i (m/s) is the velocity component in the i direction, ρ (kg/m³) is the fluid density, p (N/m²) is the dynamic pressure, ϑ (m²/s) is the kinematic viscosity, S_{ij} (1/s) is the strain-rate tensor, τ_{ij} (m²/s²) is the subgrid-scale stress, and $S_{M,i}$ is the sink term related to vegetation drag (m/s²) further defined in Eq. (7). S_{ij} and τ_{ij} are given by:

$$\overline{S}_{ij} = \frac{1}{2}\left(\frac{\partial u_i}{\partial x_j} + \frac{\partial u_j}{\partial x_i}\right) \tag{3}$$

$$\tau_{ij} = \overline{u_i}\,\overline{u_j} - \overline{u_i u_j} \tag{4}$$

Specifically, τ_{ij} represents the effect of unresolved small-scale motion on the resolved flow, and is based on the eddy-viscosity assumption:

$$\tau_{ij} - \frac{1}{3}\tau_{kk}\delta_{ij} = -\vartheta_t\left(2\overline{S}_{ij}\right) \tag{5}$$

where ϑ_t (m²/s) is the eddy viscosity. The Wall-Adapting Local Eddy-viscosity (WALE) model, proposed by Nicoud and Ducros (1999), was chosen as the subgrid-scale model to calculate ϑ_t.

The transport of scalars was modelled with the advection–diffusion equation (ADE), this equation uses a one-way interaction with the flow. In other words, the flow is not affected by the transport of this scalar.

$$\frac{\partial C}{\partial t} - \nabla \cdot (\mathrm{U}C) - \nabla^2(D_T C) = 0 \tag{6}$$

where C is the tracer concentration (transported scalar) and $D_T = 1.111$ is the constant diffusion coefficient divided by the fluid density. Furthermore, the value of C was bounded from 0 to 1 in order to represent a percentage of tracer in the domain.

2.2. Numerical model

Simulations were conducted using the open-source software Open-FOAM (version 1912). The governing equations, including conservation of mass, momentum, and energy, were discretized using the pimple-Foam module, which is known for its efficient implementation of the finite volume method (FVM) in a transient formulation. This approach

allowed us to accurately capture the transient behavior of the flow and its interactions with the surrounding environment. For the pressure–velocity coupling, we adopted the PIMPLE method scheme, which combines the strengths of the SIMPLE (Semi-Implicit Method for Pressure-Linked Equations) and PISO (Pressure-Implicit Splitting of Operators) schemes. This choice enabled us to achieve a robust and stable convergence of the pressure and velocity fields, crucial for accurate flow predictions. To solve the convection–diffusion equations, we employed an implicit second-order backward time-stepping scheme. Additionally, we utilized additional second-order schemes to enhance the accuracy and stability of our simulations. These choices were made to ensure reliable predictions of the transport phenomena, particularly in scenarios where scalar quantities play a significant role. The tolerance level for convergence was set to 1E-04 for both pressure and velocity residuals. This stringent criterion ensured that the iterative solver reached a highly accurate solution. Furthermore, we employed the PISO loop, which consisted of three iterations. Within each iteration, pressure corrections were performed three times within the SIMPLE loops, improving the overall accuracy of the simulations.

Distinguishing features between our numerical model and the approach proposed by Xiang et al. (2019) manifest notably through supplementary corrective measures, the establishment of mesh orthogonality facilitated by the incorporation of a porous medium, and the distinct formulation of the inlet boundary condition. Additionally, our model demonstrates reliance upon an openly accessible software suite as opposed to a proprietary software solution, characterizing a departure from prior methodologies.

The mass exchange between the main channel and the vegetated cavity was simulated (Equation (6)) using the washout procedure, as described in Sandoval et al. (2019). This procedure consists of setting up a non-dimensional tracer concentration $C = 1$ inside the cavity and $C = 0$ in the main channel and tracking the tracer concentration in the cavity as it is transported to the main channel. This allowed for the estimation of the concentration's temporal variation within the cavity. The concentration was recorded until at least 95 % of the tracer was washed out of the cavity. The tracer was injected only after the flow transients were eliminated, which corresponds to a time greater than $150H/U$. The turbulent Schmidt number was $S_{ct} = 0.9$, as in (Gualtieri et al., 2010). Oliveira et al. (2021) showed that the effect of the turbulent Schmidt number on the mass exchange of a vegetated lateral cavity is almost negligible, while doubling the S_{ct} changes the mass exchange by 1 %.

The time increment was adaptive with a maximum Courant number of 0.9. The maximum time step size was 0.05 s, while the mean time step size was 0.001 s. The simulation ran for nearly $150H/U$ (water depth $H = 0.10$ m, and channel bulk velocity $U = 0.101$ m/s) until the transients were eliminated. The statistics were collected and averaged using the instantaneous flow fields over, at minimum, the next $350H/U$, and, at maximum, $5000H/U$ or until 95 % of the tracer mass was washed out from the cavity.

The geometry and flow conditions were chosen to match the experimental setup described in Xiang et al. (2019), so that their measurements could be used for model validation (Fig. 1). The lateral cavity was $W = 0.15$ m wide and $L = 0.25$ m long, resulting in an aspect ratio W/L of 0.6, which corresponds to a one-gyre system with one adjacent circulation (Mignot et al., 2019). The depth in the main channel and in the cavity was $H = 0.10$ m. The flow in the main channel was turbulent ($Re = HU/\nu = 9000$, where ν is the kinematic viscosity) and subcritical ($Fr = U/(gH)^{0.5} = 0.102$, where g is the gravitational acceleration), with bulk velocity $U = 0.101$ m/s at the channel inlet. The temperature was constant at $T = 293 K$. In the computational domain, x is the streamwise direction, with origin at the cavity. In the transversal direction, $y = 0$ corresponds to the cavity interface. The vertical direction z is measured from the channel bottom.

The boundary conditions set to the model were the following (Fig. 1). The bottom of the domain (z = 0 m), the walls of the main channel and the cavity were considered as no-slip surfaces. A rigid-lid assumption

was employed at the free-surface ($z = 0.10\ m$), this simplification is a common practice in CFD and is generally accepted for $Fr < 0.36$ (Khosronejad et al., 2020). This approach was similar to other studies with lateral cavities in open-channel flows for Froude number less than 0.43 (Lu and Dai, 2016; Ouro et al., 2020; Xiang et al., 2019), which obtained good agreement with experimental results, at least for first-order turbulence statistics (Kara et al., 2015). Although the adoption of the Level-Set Method (LSM) to represent the air–water interface at channel flows can provide more accurate results than the rigid-lid boundary condition, the former comes at five times higher computational expense (Khosronejad et al., 2020). The longitudinal XZ plane, farField, where the main channel was restricted in the domain, was defined as a free-slip surface. The width of the main channel covered by the numerical model was only 0.30 m (the full width of the experimental main channel was 0.85 m) in order to avoid having to resolve the boundary layer near the opposite channel wall and save grid points. At this location, the effect caused by the cavity is negligible (Brevis et al., 2014), and the flow is parallel and nearly uniform, so that a free-slip symmetry condition was applied. Further, this simplification is valid since the main channel flow does not affect the development of transverse standing waves (Perrot-Minot et al., 2020).

The channel's inlet section received velocity field that corresponded to a fully developed open channel flow simulation done at the main channel geometry with identical initial flow conditions ($U = 0.101$ m/s) and periodic boundary conditions in the streamwise direction. This average incoming flow was used to generate turbulent fluctuations using the Turbulence Divergence-Free Synthetic Eddy Method (DF-SEM) approach (Poletto et al., 2013). This was an improvement in relation to the study of Xiang et al. (2019) which only considered a predeveloped velocity field. A convective boundary condition was adopted at the outlet, in which the zero-gradient condition allows the flow to exit the domain without having any backflow. The bottom of the domain, the walls of the main channel, and the cavity were considered as no-slip surfaces.

It is common practice in laboratory experiments to approximate aquatic vegetation as arrays of rigid circular cylinders, with the cylinder diameter in the scale of millimetres (Chen et al., 2012; Kim et al., 2015; King et al., 2012; Xiang et al., 2020, 2019). Computationally, arrays of cylinders require high grid discretization to account for the individual vegetation elements (de Lima et al., 2015), and the higher the vegetation density, the more complex the grid will be. To avoid such computational costs, one alternative is to model the vegetation as a porous medium (Xavier et al., 2018; Yamasaki et al., 2019, 2022), in which the flow resistance induced by the vegetation is either calculated or fitted based on cylinder-arranged vegetation experiments. This resistance generates a momentum loss that is added as a sink term in Equation (2). In our study, momentum loss was computed with the Darcy-Forchheimer (DF) model:

$$\overline{S}_{M,i} = -\left(\vartheta d + \frac{\rho|u_{jj}|}{2}f\right)u_i \tag{7}$$

in which ϑ (m^2/s) is the kinematic viscosity, d (1/m^2) is the viscosity drag coefficient and f (1/m) is the inertial coefficient. The coefficients d and f were calculated using the Ergun equation:

$$d = \frac{150}{D_p^2}\frac{(1-\epsilon)^2}{\epsilon^3} \tag{8}$$

$$f = \frac{3.5}{D_p}\frac{(1-\epsilon)}{\epsilon^3} \tag{9}$$

in which D_p (cm) is the mean particle diameter, and ϵ (=1-a) is the void fraction, with a being the vegetation density in the cavity:

$$a = \frac{nS_V}{S_{cav}} \tag{10}$$

where n is the number of vegetation cylinders, S_V (m^2) is the horizontal cross-section area of the vegetation cylinders, and S_{cav} (m^2) is the cavity area. The value of $a = 100$ % corresponds to a wall with no-slip condition.

To validate the porous model, we used the experimental data of Xiang et al. (2019), who designed a laboratory-scale model of rigid emergent vegetation using copper cylinders that were uniformly arranged in the flume cavity ($a = 0.13$ %). In the horizontal plane (flow perpendicular to the cylinders, which corresponds to the x- and y-axis), D_p was assumed as the cylinder diameter ($D_p = d_w = 1.5$ mm). In the vertical direction (z-axis), where the flow is parallel to the cylinders, D_p was calculated as the hydraulic diameter d_h (m):

$$d_h = d_w \left(\frac{4(s/d_w)^2}{\pi} - 1 \right) \tag{11}$$

in which s is the centre-to-centre cylinder spacing (s = 0.03 m in the setup of Xiang et al., 2019) and varies with a. To account for non-isotropic resistance, the approach of Oldham and Sturman (2001) was used to calculate d and f in the z-axis (see Equations (7) and (8)).

To explore the range of vegetation densities, a was varied between $a = 0$ (no vegetation) and $a = 10.65$ % and distributed in fourteen scenarios (Table 1). It was assumed that the vegetation was uniformly distributed in the cavity and that it spanned the cavity depth, similarly to emergent vegetation.

The discretization of the domain was defined with the grid uncertainty evaluation proposed by Dutta and Xing (2018). Three grids were employed: a coarse grid with 639,680 elements, a medium grid with 1,408,000 elements, and a fine grid with 3,132,800 elements. The refinement rate between the grids was 1.40. The numerical error was estimated using the method outlined by Dutta and Xing (2018) and was equal to 2E-05 m/s. All three-grid simulated ensemble-averaged streamwise velocities showed good agreement with the experimental results of Xiang et al. (2019) (Fig. 2). The medium grid was chosen for the simulations, presenting 1.74 % of uncertainty compared to the experimental results. The chosen grid had the lateral cavity discretised in 80X80X40 elements, in the streamwise (x-axis), spanwise (y-axis), and vertical direction (z-axis) respectively (Fig. 3). Likewise, the main channel was divided into 120X120X40 elements. The maximum time-averaged non-dimensional wall distance in the domain was y$^+$ = 5.93 in the spanwise direction and z$^+$ = 1.99 in the vertical direction, and the spatial-averaged distances were y$^+_{ave} \approx 1.64$ and z$^+_{ave} = 0.68$. Thus, the first grid off the wall is within the viscous sub-layer in the domain. The simulation was calculated on 48 cores [2 x Intel Xeon E5-2670v3 (Haswell) at a base clock of 2.3 GHz] in average 100 s of the flow was calculated in 15.58 h of real time. The fastest simulation (a = 0 %) ran in approximately 55 h and the longest (a = 10.65 %) in 442 h.

3. Results and discussion

3.1. Validation of the porous media model

Validation of the porous media model using turbulence statistics was not possible, as Xiang et al. (2019) only provided quantitative data for the average streamwise velocity. In order to enhance confidence in our porous media model, we also employed a cylinder-based representation of the vegetation inside the cavity, following the approach of Xiang et al. (2019). Fig. 4 illustrates the comparison between the two methods for representing the vegetation within the cavity. It can be observed that the most significant flow characteristics of interest in this study (e.g., flow circulation pattern and regions of low turbulent kinetic energy (TKE)) were successfully captured using the porous media simulation. However, the porous media model was unable to reproduce the small-scale turbulence characteristics near the cylinders. Our results also demonstrated qualitative agreement with the contours presented by Xiang et al. (2019) (e.g., turbulent kinetic energy contours in Fig. 6 of their paper), particularly in terms of the regions of elevated TKE within the mixing layer between the main channel and the cavity, as well as inside the cavity, in terms of magnitude and general distribution. Finally, it is worth noting that although the model has been validated for the hydrodynamic aspect, it has not undergone validation for mass transport.

3.2. Flow hydrodynamics

Fig. 5 shows streamlines of the time-averaged horizontal flow and its magnitude $\sqrt{u^2 + v^2}/U$ inside the cavity at $z/H = 0.6$ for all vegetation densities. The flow in the main channel goes from left to right. For $a = 0$ to 0.66 % (Fig. 5a–e), a primary anti-clockwise gyre was formed in the cavity, accompanied by a small secondary gyre near the upstream inner corner. Since the secondary gyre had no direct contact with the main channel, it was driven by momentum transfer from the primary gyre. The outer parts of the recirculation zones had high velocities, while the inner areas of the recirculation regions had extremely low velocities. As vegetation density in the cavity increased, the centre of the main gyre shifted towards the cavity-channel interface at the downstream corner and lost its shape (Fig. 5a–f), as also seen in Xiang et al. (2019). A transition in flow pattern was observed from $a = 1.99$ to 3.99 % (Fig. 5g–j). For $a > 3.99$ % (Fig. 5k–n), two gyres in direct contact with the main channel could be observed. The upstream gyre was anti-clockwise, while the downstream gyre was clockwise. As vegetation density continued to increase, the downstream gyre grew, occupying most of the interface between the main channel and the cavity (Fig. 5k–n). The velocity magnitude was almost zero very close to the interface ($y/W < 0.2$) as a consequence of increasing flow blockage. The increase of the vegetation density tends towards an asymptote as $a =$
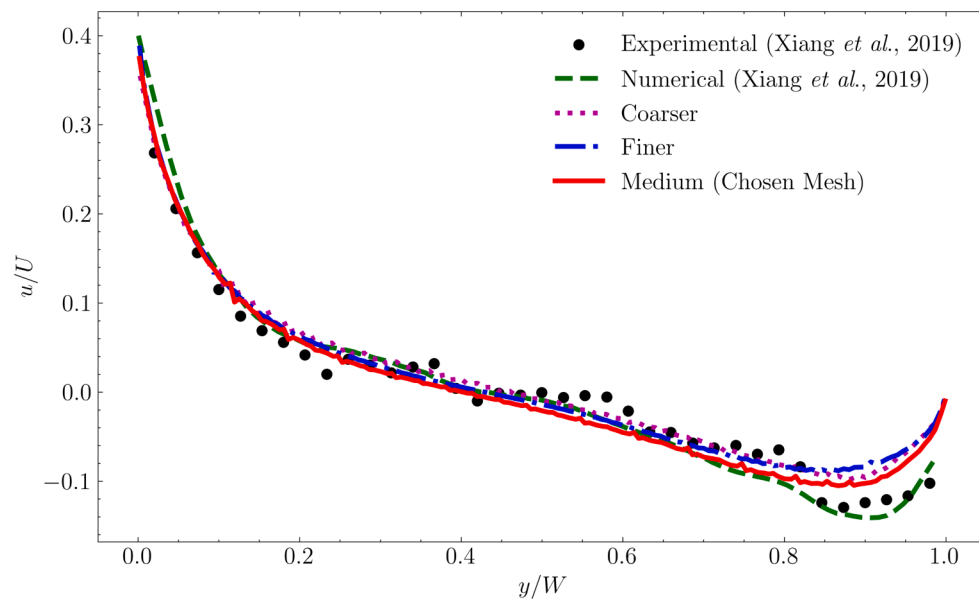
Table 1

Vegetation levels and the calculated Darcy-Forchheimer coefficients, where a (%) is the vegetation density, d (1/m2) is the viscosity drag coefficient, f (1/m) is the inertial coefficient and d_h (m) is the hydraulic diameter. Spatially averaged values of Peclet number for each vegetation.

Case	a (%)	Horizontal direction (x and y-axis)		Vertical direction (z-axis)			Peclet
		d (1/m^2)	f (1/m)	d_h (m)	d (1/m^2)	f (1/m)	Spatially averaged
0	0	0.00	0.00	0.00	0.00	0.00	1.87
1	0.13	116.53	3.09	0.7624	0.0004	0.006	1.48
2	0.16	182.25	3.87	0.8265	0.0006	0.007	1.29
3	0.33	753.83	7.89	0.3902	0.0111	0.03	1.06
4	0.66	3002.72	15.82	0.1846	0.198	0.19	0.79
5	1.33	12344.01	32.40	0.0836	3.98	0.58	0.55
6	1.99	28276.04	49.53	0.0515	23.96	1.44	0.42
7	2.66	51244.51	67.36	0.0360	88.96	2.81	0.34
8	3.33	81917.57	86.06	0.0269	254.97	4.80	0.29
9	3.99	120314.00	105.38	0.0210	613.12	7.52	0.25
10	4.66	167095.86	125.49	0.0169	1314.11	11.13	0.25
11	5.32	223190.20	146.57	0.0139	2602.53	15.83	0.21
12	7.99	546724.99	239.43	0.0072	23702.83	49.85	0.17
13	10.65	1061150.94	348.58	0.0041	140829.09	126.99	0.14

Fig. 2. Ensemble-averaged streamwise velocity in the cavity at $z/H = 0.6$ for a $= 0.13$ % (the x direction was spatially averaged into a single value), where U is the bulk velocity in the main channel and W is the cavity width. $y/W = 0$ is at the interface between the lateral cavity and the main channel. The maximum difference between numerical and experimental results was 1.74 %. Coarse grid, with 639,680 elements (dotted magenta line); medium grid, with 1,408,000 elements (solid red line); fine grid, with 3,132,800 elements (dot-dashed blue line). (For interpretation of the references to colour in this figure legend, the reader is referred to the web version of this article.)
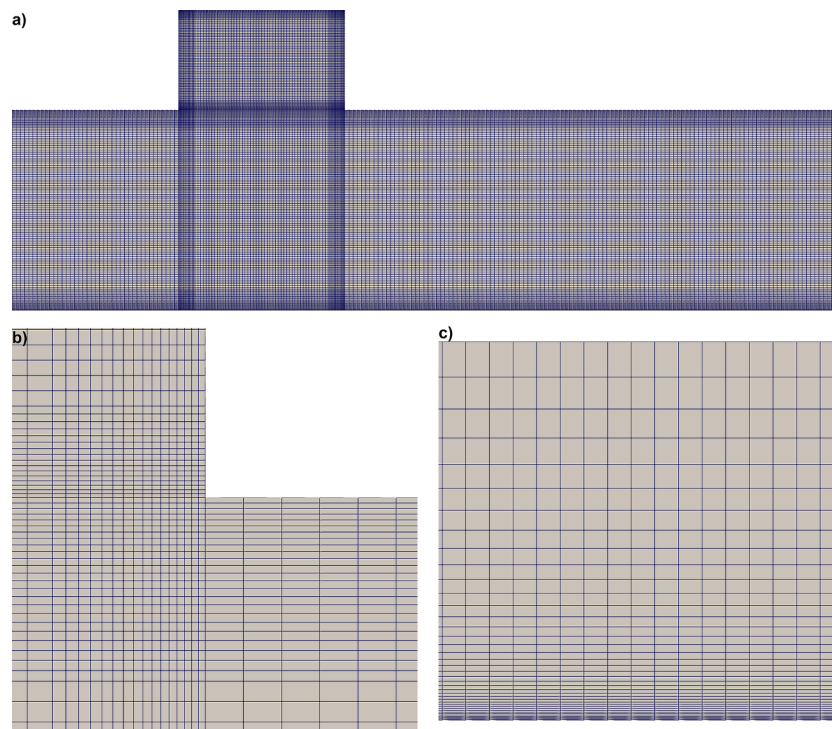

Fig. 3. Computational grid in all cases: a) mesh in the free-surface plane, b) mesh in a horizontal plane near at the downstream portion of the interface and c) mesh in the vertical plane.

100 % corresponds to a wall with the no-slip condition, which is the reason for the low velocity magnitudes as the vegetation density increased.

The time-averaged horizontal velocity field (contour plot and streamlines) in the cavity for different vegetation densities near the free surface, near mid-depth, and near the bottom, demonstrated the non-uniformity of the velocity over the depth (Fig. 6). At the bottom of the

cavity, flow velocities were in general lower than the rest of the depth due to the presence of the no-slip wall. The flow pattern in general was the same over depth, but the centre of the recirculation region shifted its position.

The non-uniformity in the flow was more pronounced at the interface between the main channel and the cavity. If close to the bottom and the free surface, the flow was predominantly oriented from the channel
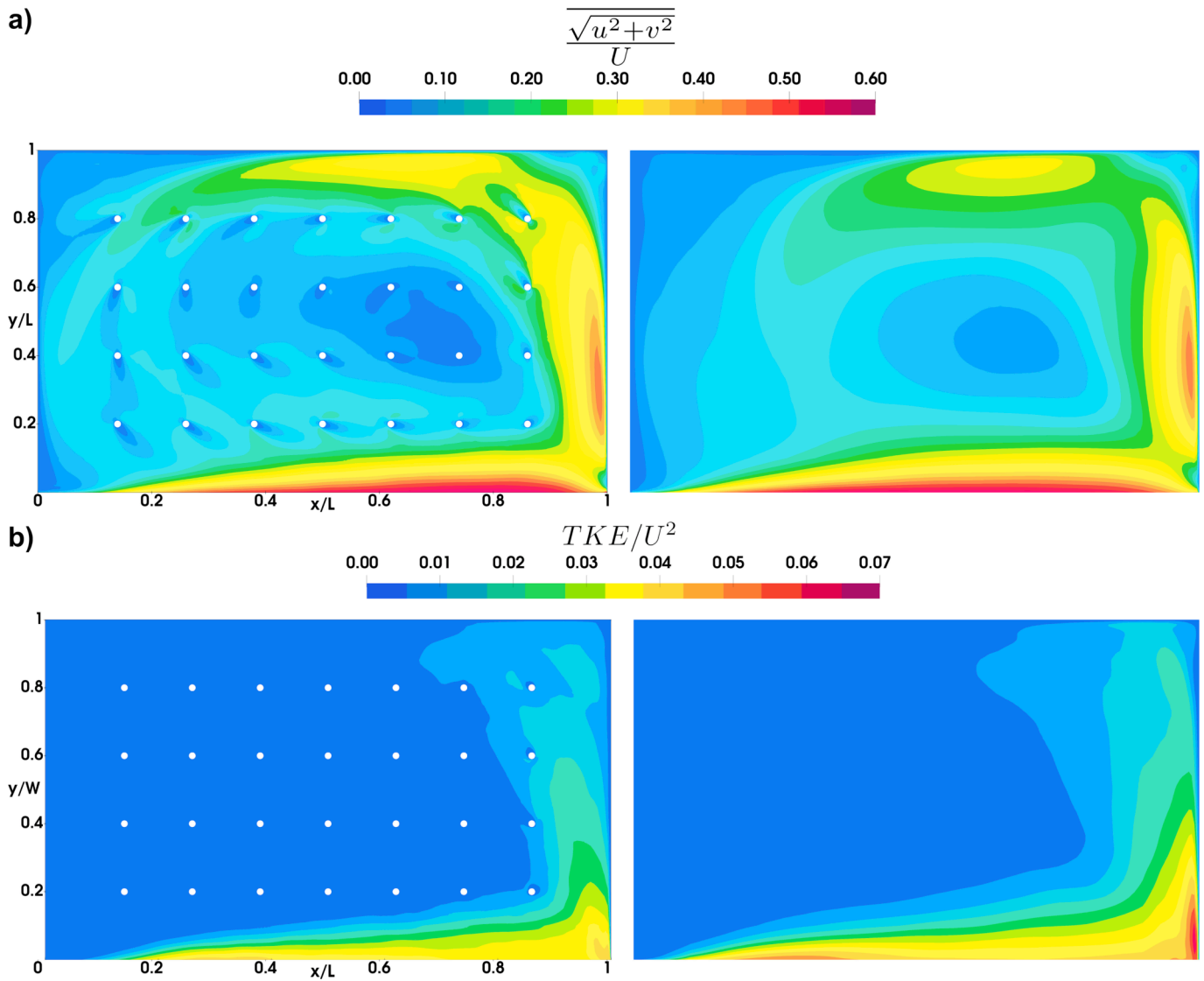
Fig. 4. Comparison of the representation of the vegetation inside the cavity using porous media model and cylinders. (a) Time-averaged superficial velocity contours at $z/H = 0.6$, and (b) TKE contours at $z/H = 0.6$. On the left the cylinders configuration and on the right the porous media configuration.

toward the cavity (Fig. 7). Between the bottom and the free surface, the transverse velocity was oriented predominantly from the cavity toward the channel over most of the interfacial length (Fig. 7). The non-vegetated case was consistent with Engelen et al. (2021). For the cases with non-vegetation and low vegetation density (Fig. 7a,b), this trend was reversed at the downstream part of the cavity, while for the cases with high vegetation density (Fig. 7d–f), this trend was reversed at the upstream part of the cavity. As vegetation density increased, the magnitude of the entrance velocity gradually decreased due to the blocking effect of the vegetation.

The shear or mixing layer is formed by the velocity gradient that exists across the interface of the main channel with the cavity. The thickness δ (m) of this mixing layer (Mignot et al., 2016) is defined as:

$$\delta = \frac{u_m(x) - u_c(x)}{|\partial u/\partial y|_{max}} \qquad (12)$$

where, u_c and u_m (m/s) are the time-averaged streamwise velocities at the interface, in the cavity and the main channel. These velocities were extracted where the velocity gradient was negligibly small, i.e., lower than 0.5 s^{-1} (Mignot et al., 2016; Xiang et al., 2020). $|\partial u/\partial y|_{max}$ represents the maximum velocity gradient at each x position along the

interface. Fig. 8a shows the evolution of the ensembled averaged thickness layer in the streamwise direction. Firstly, the thickness layer was spatially averaged along the y-axis and further, it was averaged along the depth (z).

Overall, the mixing layer increased in the downstream direction for $x/L < 0.8$. For $x/L > 0.8$ the thickness of the shear layer decreased due to a local increase of the maximum velocity gradient, a consequence of the presence of an adverse pressure gradient near the downstream corner of the cavity, which is consistent with the observations of Mignot et al. (2016) and Xiang et al. (2020) for groyne fields. The increase in the vegetation density diminished the thickness of the mixing layer, due to the increasing blockage that limited the entrance of flow into the cavity (Fig. 8 a, b). This phenomenon was notably evident for $a > 3.99$ %, whereby growth inhibition occurred within a delimited segment of the cavity width ($\delta/W < 0.05$). Moreover, the predominant trend adhered to the maximal thickness, as the mixing layer became constrained to the vicinity of the interface region. These findings suggest that the presence of vegetation in cavities influences the characteristics of the shear layer at the interface between the main flow and the cavity, similar to the observations made by Xiang et al. (2020) in groyne fields. It is worth noting that extrapolating the experimental results by Sukhodolov et al. (2017), at the same density $a = 0.13$ %, we found that vegetation
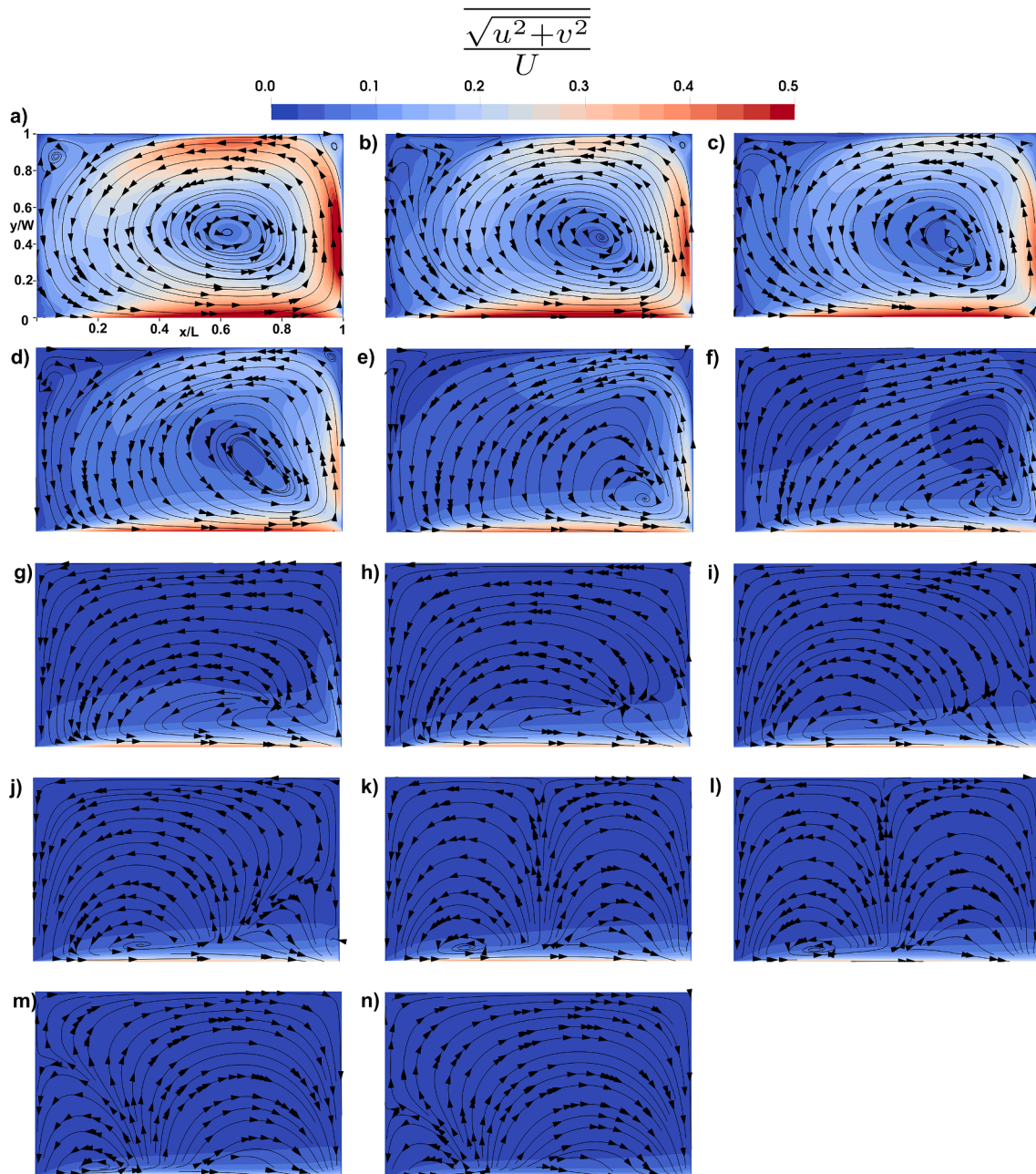
Fig. 5. Mean 2D streamlines of different vegetation densities at the horizontal plane $z/H = 0.6$ inside the cavity volume: a) $a = 0$, b) $a = 0.13$ %, c) $a = 0.16$ %, d) $a = 0.33$ %, e) $a = 0.66$ %, f) $a = 1.33$ %, g) $a = 1.99$ %, h) $a = 2.66$ %, i) $a = 3.33$ %, j) $a = 3.99$ %, k) $a = 4.66$ %, l) $a = 5.32$ %, m) $a = 7.99$ % and n) $a = 10.65$ %.

decreased in 12 % the thickness of the mixing layer, compared to the non-vegetated case. A comparable decrease of 18.9 % was observed, in the present numerical study, while for higher densities the reduction was higher.

Fig. 9 shows the time-averaged vorticity magnitude (normalised by U/H) at $z/H = 0.6$. The vorticity magnitude Ω (s^{-1}) is defined as:

$$\Omega = \nabla \times \vec{u} \qquad (13)$$

The vorticity remained high along the shear layer (Fig. 9), indicating the production of high turbulent energy (Juez et al., 2018a), and the presence of coherent structures (Mignot and Brevis, 2020; Xiang et al., 2020). The vortical structures grew along the shear layer, impinging on the downstream edge of the cavity, resulting in the entrainment of vorticity into the cavity. The vorticity in the upstream region ($x/L < 0.3$) was much greater than in the downstream region ($x/L > 0.3$). Xiang

et al. (2020) attributed this greater vorticity at the upstream region to the presence of small-scale eddies that are generated by the high velocity gradient between the cavity and the main channel with high rates of rotation. As observed further by Xiang et al. (2020), the vorticity decreased as these eddies merged and migrated downstream, and as low-vorticity water from the inside of the cavity was introduced into them. Since with the increase in vegetation density, the momentum exchange across the interface diminished, only a smaller amount of low-vorticity water entered the shear layer from the cavity, enhancing the interfacial vorticity. This result is consistent with that observed by Xiang et al. (2020) for groyne fields. Inside the cavity, higher vorticities were attached to the wall, particularly on the downstream wall. As the vegetation density increased, the levels of vorticity inside the cavity decreased. For $a = 10.65$ % (Fig. 9 d), for example, the vorticity inside the cavity was almost zero.
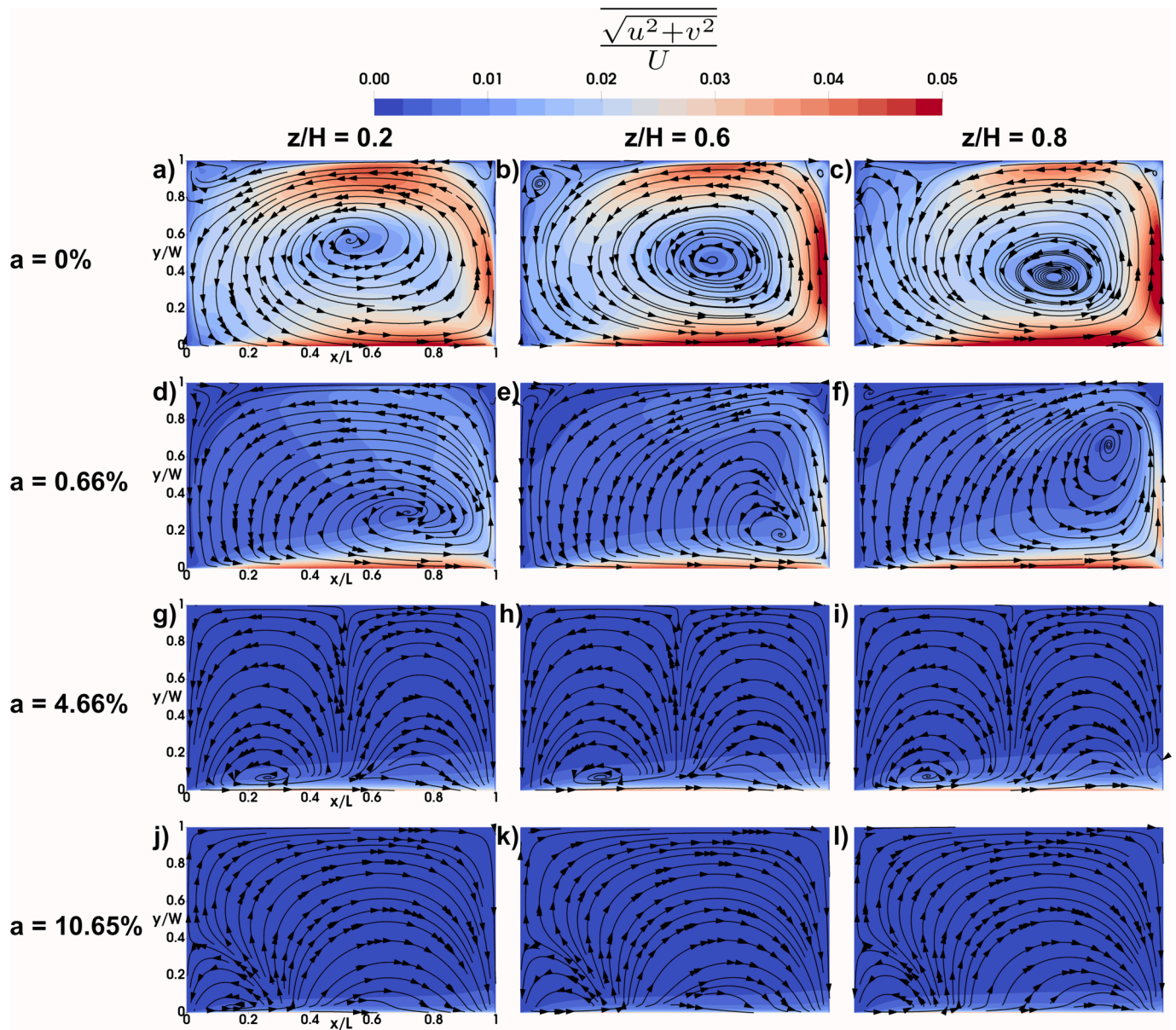
Fig. 6. Mean 2D streamlines of different vegetation densities at $z/H = 0.2$, 0.4 and 0.8, inside the cavity volume and contour of the time-averaged velocity at the interface: a) $a = 0$, b) $a = 0.66$ %, c) $a = 4.66$ % and d) $a = 10.65$ %.

The turbulent kinetic energy (TKE) in a LES simulation is defined as:

$$TKE = 0.5tr(R) + 0.5tr(u^{'}) \qquad (14)$$

where tr is the trace operation (sum of all the main diagonal terms of the Resolved and Modelled Reynolds Stress Tensor), R (m²/s²) is the modelled Reynolds stress tensor and $u^{'}$ (m²/s²) is the resolved Reynolds stress tensor. A time averaged TKE distribution, normalised by U^2, is presented in Fig. 10. The values of TKE remained high throughout all interface, compared to the cavity volume, due to strong shear and turbulence at the shear layer, and an intermittent process of coherent structures entrance along the interface (Mignot and Brevis, 2020; Sandoval et al., 2019). The lower density cases ($a < 0.66$ %) presented higher TKE inside the cavity due to the additional Kelvin-Helmholtz (KH) instabilities at the shear layer between vegetation and the main channel (Nepf, 2012b; Xiang et al., 2019). For $a > 0.66$ %, the momentum dissipation imposed by the vegetation limited the growth of the shear layer inside the cavity at a higher rate than the initial KH instabilities, which led to a decrease in TKE levels. In general, the level of

TKE decreased downstream along the shear layer due to the dissipation that happens when water with low TKE is transferred from inside the cavity into the shear layer (Xiang et al., 2020). The turbulent structures that entered the cavity near the downstream edge lost TKE intensity as they were advected along the downstream wall and along the outer layer of the gyre. TKE was low inside the cavity. As vegetation density increased, the values of TKE inside the cavity decreased, being almost zero for a > 3.99 % (Fig. 10 c and d). This is due to the increased drag force of vegetation, which drops the high turbulent vortices carried by the inlet flow.

In summary, vegetation density significantly influences the hydrodynamics of flow within a cavity. Low vegetation density induces a prominent single gyre pattern within the cavity, while high vegetation density exhibits a dual gyre pattern. Sparse vegetation facilitates full penetration of cavity flow, whereas dense vegetation almost entirely isolates the cavity from the main channel flow, with only a small connected region near the interface. The mixing layer thickness is greater for low vegetation density than for high vegetation density. Sparse vegetation generates flow with pronounced vorticity and turbulent
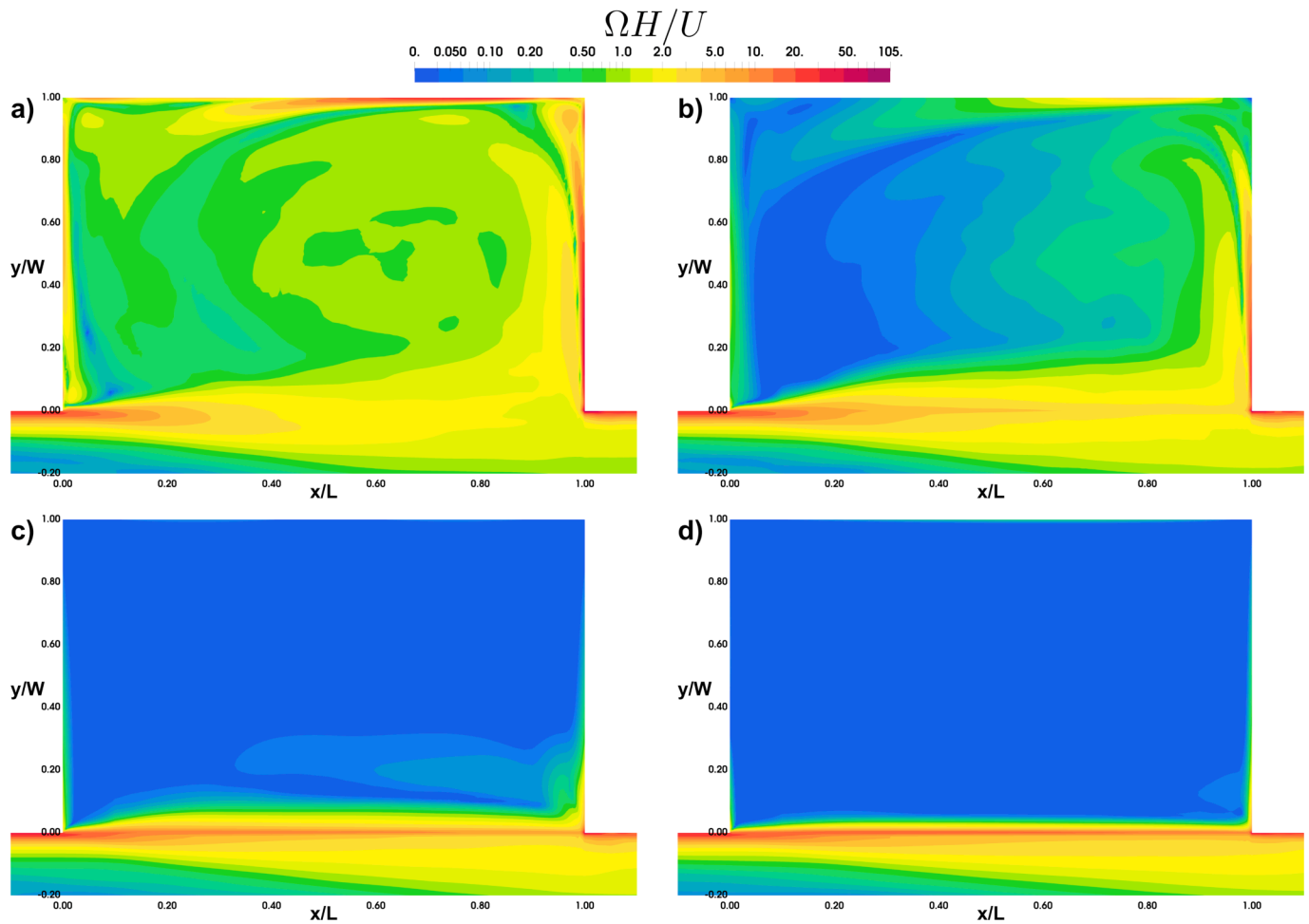
Fig. 7. Time-averaged velocity (y-direction) contour of the transversal velocity along the interface plane: a) $a = 0$, b) $a = 0.13$ %, c) $a = 0.66$ %, d) $a = 3.99$ %, e) $a = 4.66$ % and f) $a = 10.65$ %.

Fig. 8. Longitudinal distribution of the ensemble averaged mixing layer thickness spatially averaged at the z-axis.

kinetic energy (TKE) within the cavity, whereas dense vegetation leads to nearly negligible vorticity and TKE. As will be elucidated in the subsequent sections, this distinctive hydrodynamic behaviour for cavities with low and high vegetation density has implications for solute transport across the cavity/main channel interface, sediment transport, and channel resistance. Further investigations are warranted to explore the versatility of this threshold value ($a = 3.99$ %), as this study focused solely on its application under a specific flow condition and cavity design.

Nevertheless, although we did not investigate other cavity configurations (e.g., cavities with different W/L ratios), it is possible to infer

that for cavities with sparse vegetation, the influence of cavity geometry will be primary, while the influence of vegetation density will be secondary. This is because even though the intensity of velocity, turbulence, and vorticity is reduced with increasing vegetation density, the overall pattern remains approximately the same for sparse vegetation. This similar pattern of hydrodynamic behavior has also been observed in other studies, such as that of Xiang et al. (2019). In this case, for example, if the cavity has a W/L ratio between 0.6 and 2, a single recirculation pattern is expected, approximately circular and occupying the whole cavity, similar to what occurs without vegetation, but with reduced intensity of velocity, turbulence, and vorticity as vegetation

$$\Omega H/U$$

Fig. 9. Time-averaged vorticity at $z/H = 0.6$. a) $a = 0$, b) $a = 0.66$ %, c) $a = 4.66$ % and d) $a = 10.65$ %.

density increases. On the other hand, for dense vegetation, the flow is completely dominated by the resistance offered by the vegetation and is practically non-existent in the interior of the cavity, except for a very thin region near the interface. In this case, the effect of vegetation density will be of primary importance when compared to the effect of cavity geometry. Thus, if, for example, the cavity has a W/L ratio between 0.6 and 2, the geometry will only have a potential effect on the interfacial layer, but will not be relevant in the rest of the cavity.

3.3. Mass exchange between the cavity and the main channel

The interactions between the shear layer, the gyre within the cavity, and the main channel are critical in understanding mass transfer between the channel and the cavity. To characterise the interfacial mass exchange, one-dimensional transport models based on the dead zone theory were used (e.g., Uijttewaal et al., 2001). They assume exponential decay of the mean concentration (mass of tracer inside cavity) in the form:

$$C(t) = C_0 \exp(-t/T_{tracer}) \qquad (15)$$

$$k = \frac{W}{T_{tracer} U} \qquad (16)$$

where $C_0 = 1$ is the initial concentration inside the cavity, t (s) is time, T_{tracer} (s) is the characteristic decay time, and k is the nondimensional exchange coefficient related to T_{tracer}. The value of T_{tracer} was obtained by fitting Eq. (15) to the volumetric-averaged tracer concentration calculated at each timestep inside the cavity. The fitting was calculated

with a non-linear least square method (Weitbrecht, 2004) (Fig. 11 a, b). This method gives a single, unique time scale for the entire time series (Drost et al., 2014). The mean retention time increased as vegetation density increased (Fig. 13). There is a change in slope of the mean retention time for $a \approx 3.99$ %. The change in mean retention time with vegetation intensity was higher for $a < 3.99$ %, when compared with $a > 3.99$ %. For $a < 3.99$ %, the exchange velocity k drops off quickly with increasing vegetation density a. For $a > 3.99$ %, k was small, but not zero, and decreased slowly as a increased.

Using the first-order model, a single time scale fully defines the time series of concentration in the cavity. However, our results showed that the cavity can be approximated as a first-order system only for early time for $a > 3.99$ %. For late times, a second time scale was present, which was confirmed by the change in the slope of the concentration decay. This is consistent with results found in the literature (Constantinescu et al., 2009; de Oliveira and Janzen, 2020; Engelhardt et al., 2004; Kozerski et al., 2006; Gualtieri et al., 2010; Gualtieri, 2008). This behaviour was confirmed with the tracer contour at different flow times, fixed with the volumetric averaged concentrations of 75 % and 25 % that clearly indicated the different regions where the tracer cloud was trapped for both $a = 0.13$ % and 3.99 % (Fig. 12). Also, it highlights developments in tracer spread. A value of $a = 3.99$ % was the transition from advection to diffusion dominated (Peclet Number $= Hv/D_f \approx 1$, where v is the time-averaged velocity in the y-axis and D_f is the effective diffusivity). Peclet numbers were computed individually at the centre of each cell, subsequently undergoing an averaging process within the lateral cavity. Thus, the exchange process cannot be represented completely as a first-order system, being necessary at least a two-zone
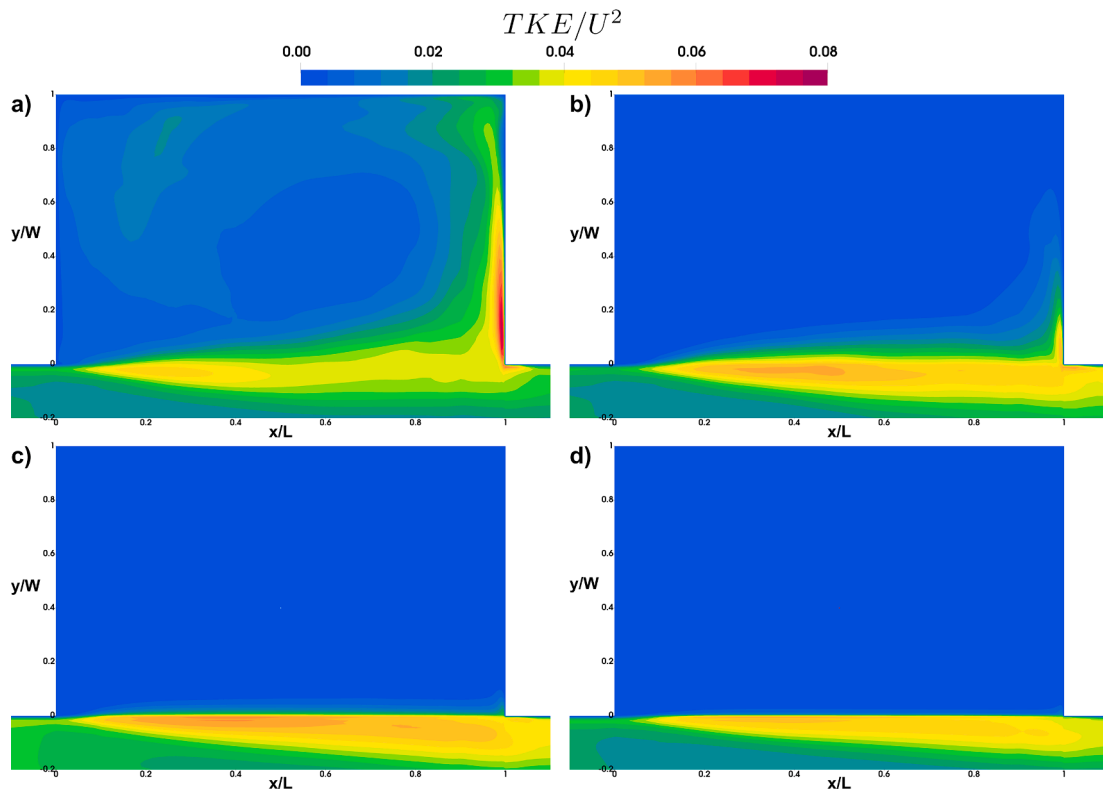
Fig. 10. Time-averaged turbulent kinetic energy at $z/H = 0.6$. a) $a = 0$, b) $a = 0.66$ %, c) $a = 4.66$ % and d) $a = 10.65$ %.
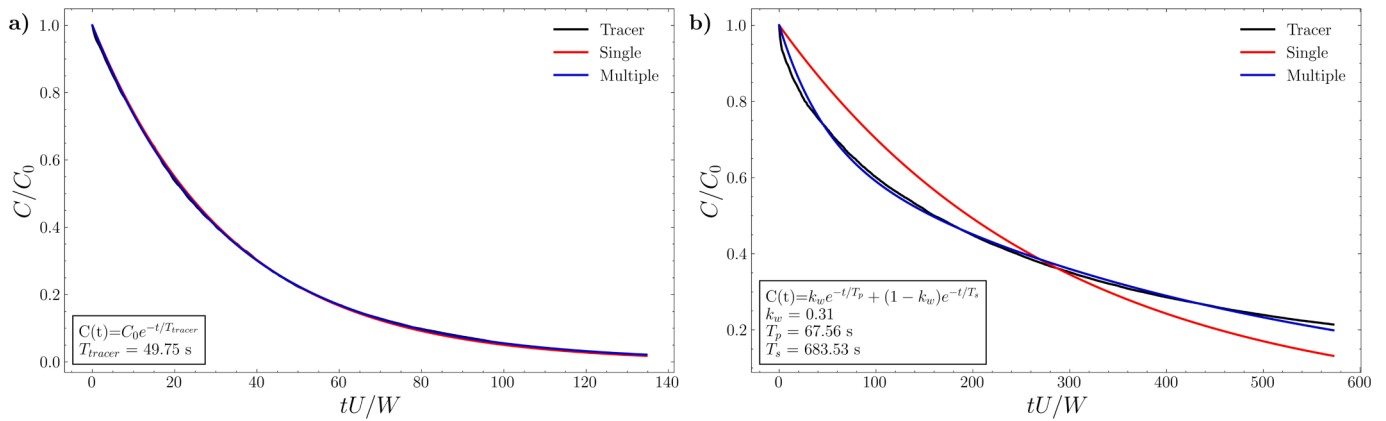

Fig. 11. Volumetric-averaged tracer concentration decay inside the lateral cavity vs time: a) a = 0.13 % and b) a = 3.99 %.

model (Fig. 11 b). Drost et al. (2014) suggested that the mean concentration in the cavity could be expressed as

$$C(t) = k_w \exp\left(-t/T_p\right) + (1 - k_w)\exp(-t/T_s) \tag{19}$$

where k_w is a weighting factor, T_p (s) is the primary time scale and T_s (s) is the secondary time scale. A SciPy Python-based global optimization code employing the bounded version of the differential evolution algorithm was employed to minimize the filtered squared difference between the tracer's temporal evolution and the two-slopes model. The secondary time scale, T_s, was 1.1 to 8.1 times larger than the primary time scale, T_p, indicating the presence of at least two distinct time scales within the cavity, as stated above, particularly for increasing values of vegetation density ($a \geq 3.99$ %) (Fig. 13). Both time scales increased with a, with the primary time scale governing mass exchange with the main channel at early times, while the asymptotic behaviour of the concentration at later times was dominated by the secondary time scale,

in alignment with Drost et al. (2014). The shift from a single slope to a two-slope tracer decay is evident at a critical threshold value of a = 3.99 %. This alignment is consistent with the rapid decrease in the Peclet number (Pe) for a ≤ 0.33 %, signifying advection-dominated transport, and the slower decrease for a > 3.99 %, indicating diffusion-dominated transport (Table 1). Notably, this threshold of vegetation density holds potential as an informative indicator for river managers, highlighting the importance of undertaking maintenance actions to ensure the effectiveness of mass exchange processes.

Fig. 13 highlights the variation of the mean retention time with increasing vegetation density (a). Similar to Xiang et al. (2019), there was a deviation in the mean retention time curve near a ≈ 0.33 %, which was associated with the plant-induced Karman vortex street and Kelvin-Helmholtz (KH) eddies (Nepf, 2012b). These phenomena resulted in a decrease in the k decay rate, with vegetation blockage emerging as the dominant factor. These findings align with the measurements of
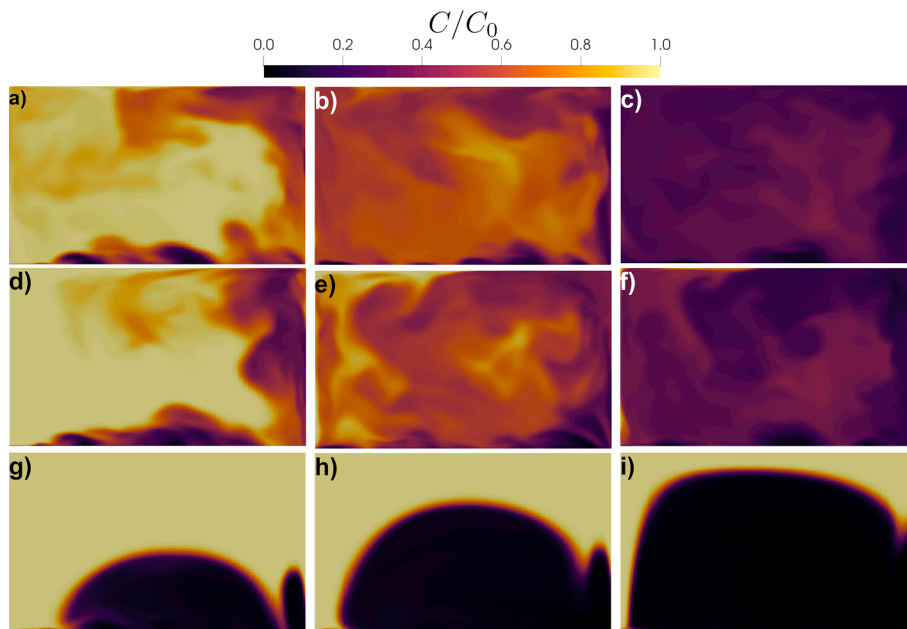
Fig. 12. Tracer fields with the volumetric averaged concentration of 75 %; a) a = 0, d) a = 0.13 % and g) a = 3.99 %, 50 %; b) a = 0, e) a = 0.13 % and h) a = 3.99 %; and 25 %; c) a = 0, f) a = 0.13 % and i) a = 3.99 %.
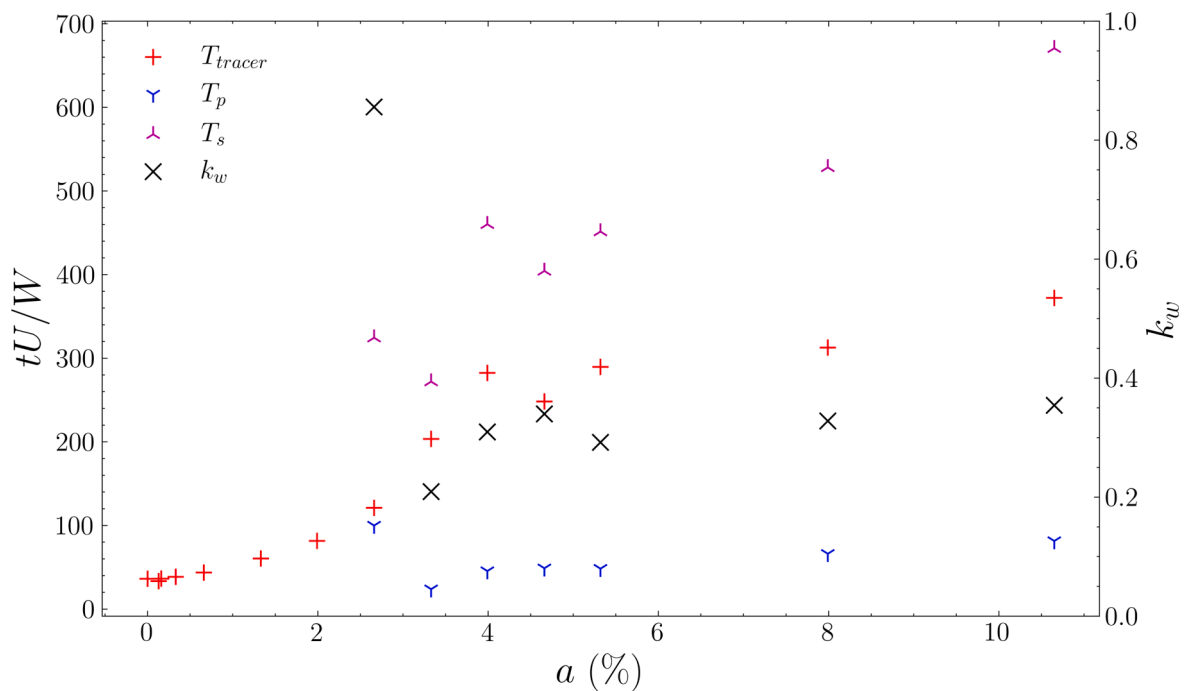

Fig. 13. Mean retention time vs vegetation density, where T_{tracer} is the globally adjusted function, T_p is the primary mass exchange in the two-slopes adjusted function and T_s is the secondary mass exchange in the two-slopes adjusted function.

dissolved oxygen exchange between the main channel and cavity for various cavity aperture areas reported in Sanjou et al. (2018).

The variation of residence time with vegetation density is an important result of this study. The phytoplankton growth, for example, is directly related to retention time in dead zones (Engelhardt et al., 2004). Low residence times may not be sufficiently long for the maintenance of local phytoplankton reproduction, while high residence times may enhance phytoplankton abundance (Engelhardt et al., 2004). Reynolds et al. (1991), for example, reported concentrations of alga chlorophyll up to 40 times higher in a dead zone than in the main

channel of the River Severn, UK; while Engelhardt et al. (2004) observed retention time values which were insufficient for significant phytoplankton growth. Hence, cavities with low vegetation density and residence time could not be appropriate for phytoplankton growth; but as the vegetation density increases, and consequently the residence time, the cavity would be more promising for phytoplankton growth.

Finally, the increase in vegetation density may affect water quality inside the cavity since it affects both the residence time inside the cavity and at the rate of mass supply from the main channel to the vegetation inside the cavity. The longer pollutants remain in the cavity, the more

pollutants are removed through the vegetation. In this case, cavities with vegetation with higher density could remove more pollutants. However, mass removal within the vegetated cavity is also influenced by the amount of mass supplied to the vegetation inside the cavity. As the mass exchange decreases toward zero with the increase of vegetation density, even though the residence time can become very long, the mass removed by the vegetation will approach zero, because no mass is delivered into the vegetated cavity.

3.4. Sediment deposition

Regions of sediment deposition are frequently associated with regions of diminished TKE and velocity. Ouro et al. (2020), for example, found a correlation between low TKE levels and vertical velocity and sediment deposition in channel lateral bank cavities. Specifically, sediment deposition was observed where the absolute value of z-velocity (w) was below 1 % of the bulk velocity (-0.01 < w/U < 0.01). Additionally, Ouro et al. (2020) observed that these deposition areas tended to coincide with regions characterized by low turbulent kinetic energy (TKE) values. The criterion for defining "small" TKE values was derived from our analysis based on Fig. 15 of Ouro et al. (2020), where TKE/U2 was generally found to be $\lesssim 0.003$ at the horizontal plane XY at z/H = 0.01. These velocities and TKEs were connected to a mean sediment diameter of 0.2 mm, which is in the range of non-cohesive fine sediment, 0.062–0.5 mm, and can be found, for example, in the Rhone River (Juez et al., 2018a). The sediment density was 1,160 kg/m^3. In scenarios characterized by dense vegetation, a supplementary criterion has been introduced to delineate the region of sediment deposition. Given that velocity fails to penetrate beyond approximately 0.20 W from the interface, sediment deposition is correspondingly constrained within this specified distance. Fig. 14 displays the computed deposition area across varying densities of vegetation, wherein regions of deposition are denoted by the colour black. Notably, the introduction of an supplementary criterion for sedimentation is manifested by a delineating red line, serving to demarcate the sector in which sedimentation is exclusively permissible below said demarcation. The increase of vegetation density resulted in settling of sediment throughout almost the entire cavity. For a > 2.66 %, the only region where the TKE levels were high enough to prevent settling was in the inner mixing layer, which

gradually diminished with the increase of vegetation density (Fig. 8). In the non-vegetated case, the sediment deposition occurred mainly at the centre of the gyre, in accordance with (Juez et al., 2018a,b; Sukhodolov et al., 2002). It is important to note that we interpreted the flow pattern (vertical velocity and turbulent kinetic energy) in terms of implications for deposition, but there are other factors that play a significant role in sediment deposition, such as bed morphology, flow regime, seasonal and climatic variations, and biological interactions. Our findings add to the investigations by de Oliveira et al., (2022a), where they systematically demonstrated the consistent influence of vegetation on sediment transport patterns and motion characteristics within the entire cavity. Their study revealed a persistent correlation between increased vegetation density and the facilitation of sediment deposition or restriction of movement within the cavity. This observed correlation is not universally evident across all sediment grain sizes in a vegetation-free cavity. As posited by de Oliveira et al., (2022a), the presence of vegetation enhances the protective mechanism against sediment mobilization, potentially making substantive contributions to the maintenance of main channel depths and the entrapment of contaminants adhered to sediment particles. Furthermore, sediment transport is also affected by the shape of the lateral cavity, both in non-vegetated conditions (de Oliveira et al., 2022b) and vegetated conditions (de Oliveira et al., 2023b). These studies showed that regardless of the shape of the lateral cavity, the presence of vegetation continues to facilitate sediment deposition.

3.5. Flow resistance

The bed shear stresses in relation to the transverse distance for different vegetation densities within the cavity are illustrated in Fig. 15a. At the interface, the bottom shear stress rises rapidly from its low value within the cavity to a peak in the main channel immediately after the interface. The maximum bottom shear stress value is lower for cavities with sparse vegetation compared to cavities with dense vegetation. Beyond the peak, as one moves away from the interface and into the main channel, the bottom shear stress slightly decreases, then rises again towards its value within the main channel "core".

The presence of the cavity results in an average increase in bottom shear stress ranging from 0 to 1.5 times that of a channel without a
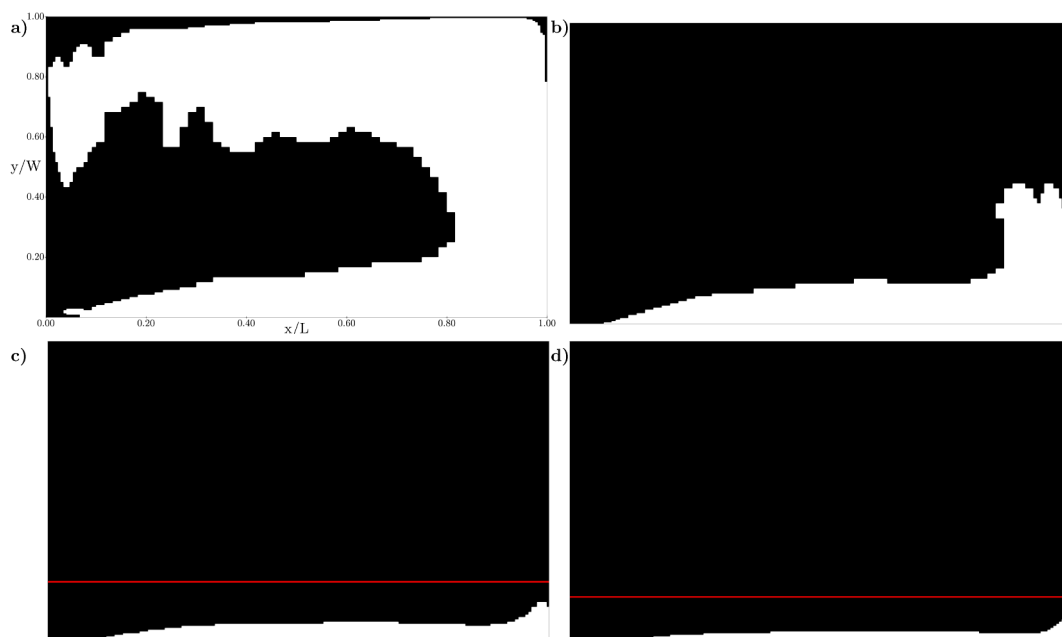

Fig. 14. Estimates of the sedimentation fields based on the Turbulent Kinect Energy (TKE) and on the *z-axis* velocity (w). Sedimentation occurs in black areas below the red line. a) $a = 0$, b) $a = 0.66$ %, c) $a = 2.66$ % and d) $a = 5.32$ %.
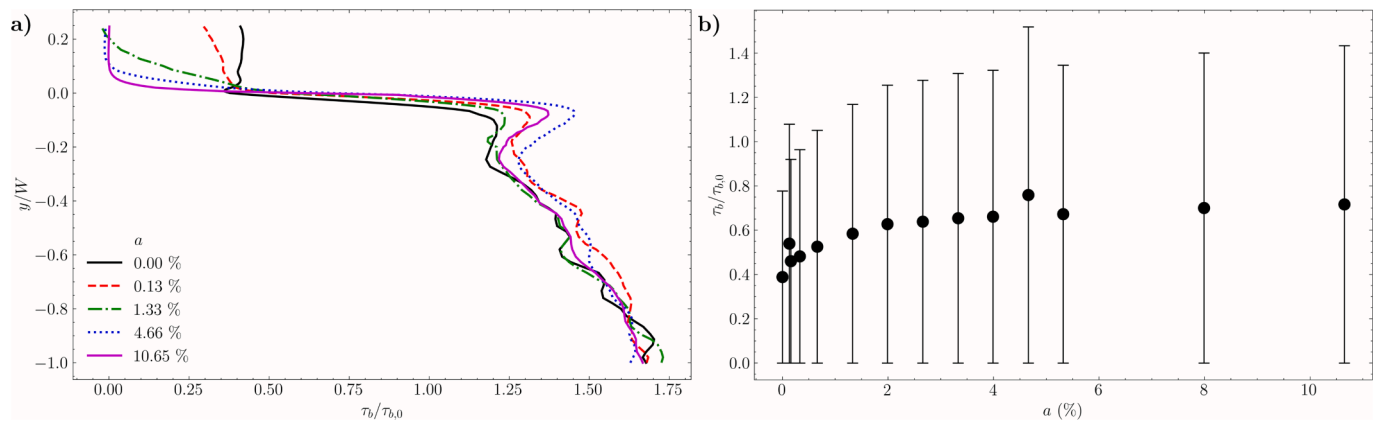
Fig. 15. Bed shear stresses a) as a function of transverse distance for varying vegetation densities and b) averaged bed shear stress versus density at the interface. All bed shear stress values have been non-dimensionalised with respect to those observed in a channel characterised by equivalent flow conditions, albeit lacking a lateral cavity.

cavity (Fig. 15b). As vegetation density within the cavity increases, the bottom shear stress experiences a rapid rise until a density of 1.99 %, at which point its value becomes constant. Our findings are consistent with the results obtained by Valyrakis et al. (2021), who investigated the impact of increasing riverbank vegetation density on flow dynamics in an asymmetrical channel. They observed a progressive overall rise in near-bed shear stresses with increasing riverbank vegetation densities. For example, for vegetation densities ranging between 0.06 % and 0.08 %, the bed shear stress was 1.17 times that of the case without vegetation, and for densities between 0.55 % and 0.99 %, the bed shear stress was 1.48 times that of the case without vegetation. These outcomes illustrate that the presence of the cavity, along with the enclosed vegetation, leads to the redistribution of flow across the cross-section, inducing changes in bottom shear stress. These results demonstrate an increased likelihood of bed material transport within the main channel as vegetation density increases inside the cavity. Such processes could contribute to the deepening of the main channel.

Furthermore, in the absence of a cavity, an additional source of resistance emerged from the lateral wall at the precise location where the cavity was subsequently introduced. Conversely, in the scenario featuring a cavity, the prevailing flow resistance can be attributed to the interfacial shear stress at the junction between the cavity and the main channel. The introduction of the cavity imparts a pronounced increase in lateral stress, surpassing the lateral stress within a cavity-free channel by more than 11-fold (Fig. 16). Furthermore, with the augmentation of vegetation density within the cavity, the lateral stress exhibits a discernible escalation, culminating upon reaching a density of 1.33 %, at

which juncture the magnitude of the interfacial shear stress attains a stable state. Consequently, the influence of cavities extends beyond the alteration of bottom flow resistance solely within the main channel; it also substantially impacts lateral flow resistance. This phenomenon designates the cavity as a significant macro-roughness structure positioned along the channel banks (Meile et al., 2011).

4. Conclusion

The current study investigated hydrodynamics, mass exchange and sediment transport in lateral vegetated cavities in an open channel. Large eddy simulations was used to calculate the hydrodynamics of the flow, the mass transport was described a tracer calculated with the advection–diffusion equation (ADE), and the sediment transport was inferred with correlations using the turbulent kinetic energy (TKE). The vegetation density was in the range from $a = 0$ to 10.65 %. It was demonstrated that vegetation density has a strong influence on hydrodynamics and mass transport. One important vegetation density threshold was identified, namely $a = 3.99$ %. Two major, different hydrodynamics and mass transfer patterns were found.

For cavities with low vegetation density ($a < 3.99$ %), we observed one primary gyre in contact with the interface between the main channel and the cavity and the velocity inside the cavity was generally high. The thickness of the mixing layer could grow longitudinally along the interface, while regions with high vorticity and turbulence kinetic energy were observed at the interface and inside the cavity. The mass transfer was governed by advection. Sediment deposition was found mainly at the centre of the gyres, regions with low vertical velocity and turbulence.

For cavities with high vegetation density ($a > 3.99$ %), we observed two primary gyres in contact with the interface between the main channel and the cavity and the velocity inside the cavity were low and near zero. The thickness of the mixing layer could not grow longitudinally along the interface, while vorticity and turbulence kinetic energy inside the cavity were low and near zero. Conclusively, the process of mass transfer was primarily dictated by diffusion mechanisms, while sediment deposition predominantly manifested across the entirety of the cavity due to the persistent low vertical velocity and turbulence. The hindrance imposed by vegetation impeded sediment mobility. Moreover, the presence of vegetation contributed to the elevation of bed shear stresses within the main channel, particularly evident in regions proximal to the interface between the main channel and lateral cavity.

This investigation has demonstrated that the presence of vegetation induces a discernible elevation in macro-roughness, consequently augmenting lateral shear stress. Notably, this augmentation attains a quasi-constant state within denser vegetation configurations. In conclusion,
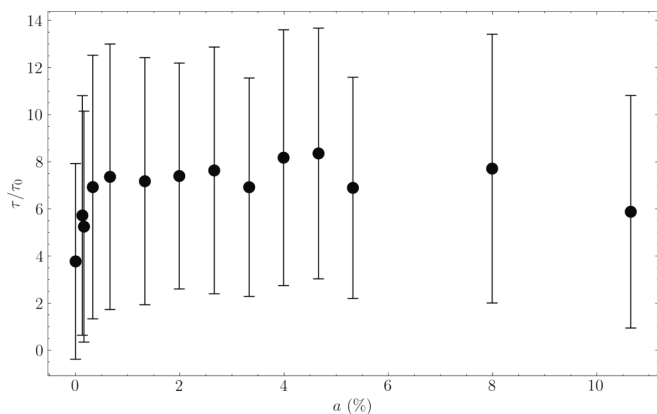

Fig. 16. Averaged shear stresses at the main channel / cavity interface as a function of vegetation densities.

this study offers valuable insights that can furnish managerial practitioners with essential guidelines, delineating the ramifications of vegetation proliferation upon the longitudinal transport of mass within natural systems.

CRediT authorship contribution statement

Luiz E. D. de Oliveira: Conceptualization, Investigation, Validation, Writing – original draft. **Taís N. Yamasaki:** Conceptualization, Methodology, Writing – original draft, Writing – review & editing. **Johannes G. Janzen:** Conceptualization, Resources, Supervision, Writing – review & editing. **Carlo Gualtieri:** Conceptualization, Supervision, Writing – review & editing.

Declaration of competing interest

The authors declare that they have no known competing financial interests or personal relationships that could have appeared to influence the work reported in this paper.

Data availability

Data will be made available on request.

Acknowledgements

References

Altai W, Chu VH (1997) Retention time in a recirculating flow. 27th congress of IAHR, 10–15 August 1997, San Francisco, pp 9–14.

Arend, K.K., Bain, M.B., 2008. Fish communities in coastal freshwater ecosystems: The role of the physical and chemical setting. BMC Ecol 8. https://doi.org/10.1186/1472-6785-8-23.

Asaeda, T., Siong, K., Kawashima, T., Sakamoto, K., 2009. Growth of Phragmites japonica on a sandbar of regulated river: Morphological adaptation of the plant to low water and nutrient availability in the substrate. River Res Appl 25, 874–891. https://doi.org/10.1002/rra.1191.

Barko, J.W., Gunnison, D., Carpenter, S.R., 1991. Sediment interactions with submersed macrophyte growth and community dynamics. Aquat Bot 41, 41–65. https://doi.org/10.1016/0304-3770(91)90038-7.

Booij R (1989) Exchange of mass in harbors. 23rd congress of IAHR, 21–25 August 1989, Ottawa, Canada, pp D69–D74.

Brevis, W., García-Villalba, M., Niño, Y., 2014. Experimental and large eddy simulation study of the flow developed by a sequence of lateral obstacles. Environ. Fluid Mech. 14, 873–893. https://doi.org/10.1007/s10652-013-9328-x.

Brodersen, K.E., Hammer, K.J., Schrameyer, V., Floytrup, A., Rasheed, M.A., Ralph, P.J., Kühl, M., Pedersen, O., 2017. Sediment resuspension and deposition on seagrass leaves impedes internal plant aeration and promotes phytotoxic H2S intrusion. Front Plant Sci 8. https://doi.org/10.3389/fpls.2017.00657.

Buczyński, P., Szlauer-Łukaszewska, A., Tończyk, G., Buczyńska, E., 2017. Groynes: A factor modifying the occurrence of dragonfly larvae (Odonata) on a large lowland river. Mar Freshw Res 68, 1653–1663. https://doi.org/10.1071/MF16217.

Chen, Z., Ortiz, A., Zong, L., Nepf, H., 2012. The wake structure behind a porous obstruction and its implications for deposition near a finite patch of emergent vegetation. Water Resour Res 48. https://doi.org/10.1029/2012WR012224.

Constantinescu, G., Sukhodolov, A., McCoy, A., 2009. Mass exchange in a shallow channel flow with a series of groynes: Les study and comparison with laboratory and field experiments. Environ. Fluid Mech. 9, 587–615. https://doi.org/10.1007/s10652-009-9155-2.

Cotton, J.A., Wharton, G., Bass, J.A.B., Heppell, C.M., Wotton, R.S., 2006. The effects of seasonal changes to in-stream vegetation cover on patterns of flow and accumulation of sediment. Geomorphology 77, 320–334. https://doi.org/10.1016/j.geomorph.2006.01.010.

de Lima, P.H.S., Janzen, J.G., Nepf, H.M., 2015. Flow patterns around two neighboring patches of emergent vegetation and possible implications for deposition and vegetation growth. Environ. Fluid Mech. 15, 881–898. https://doi.org/10.1007/s10652-015-9395-2.

de Oliveira, L.E.D., Janzen, J.G., 2020. Mass Exchange in Dead Water Zones: A Numerical Approach. In: Leal Filho, W., de Andrade Guerra, J.B.S. (Eds.), Water, Energy and Food Nexus in the Context of Strategies for Climate Change Mitigation. Springer International Publishing, Cham, pp. 59–68. https://doi.org/10.1007/978-3-030-57235-8_5.

de Oliveira, L.E.D, da Costa, F.R., Gualtieri, C., Janzen, J.G., 2022a. Effects of Vegetation Density on Sediment Transport in Lateral Cavities. Environmental Sciences Proceedings 21, 16. https://doi.org/10.3390/environsciproc2022021016.

de Oliveira, L.E.D., Gualtieri, C., Janzen, J.G., 2023a. Hydrocomplexity in Vegetated Lateral Cavities. Presented at the 40th IAHR World Congress - "Rivers - Connecting Mountains and Coasts," Vienna, Austria, pp. 3134–3141. https://doi.org/10.3850/978-90-833476-1-5_iahr40wc-p0719-cd.

de Oliveira, L.E.D., Gualtieri, C., Janzen, J.G., 2023b. Effect of Geometric Shapes on Vegetated Lateral Cavities. Presented at the 40th IAHR World Congress - "Rivers - Connecting Mountains and Coasts," Vienna, Austria, pp. 52–61. https://doi.org/10.3850/978-90-833476-1-5_iahr40wc-p0043-cd.

de Oliveira, L.E.D., Janzen, J.G., Gualtieri, C., 2022b. Effects of Geometric Shapes on the Hydrodynamics and Sediment Transport in Lateral Cavities. In: Presented at the 39th IAHR World Congress. Granada. https://doi.org/10.3850/IAHR-39WC2521716X20221064.

Drost, K.J., Apte, S.v., Haggerty, R., Jackson, T., 2014. Parameterization of Mean Residence Times in Idealized Rectangular Dead Zones Representative of Natural Streams. J. Hydraul. Eng. 140, 04014035. https://doi.org/10.1061/(asce)hy.1943-7900.0000879.

Duró, G., Crosato, A., Kleinhans, M.G., Roelvink, D., Uijttewaal, W.S.J., 2020. Bank Erosion Processes in Regulated Navigable Rivers. J Geophys Res Earth Surf 125. https://doi.org/10.1029/2019JF005441.

Dutta, R., Xing, T., 2018. Five-equation and robust three-equation methods for solution verification of large eddy simulation. J. Hydrodyn. 30, 23–33. https://doi.org/10.1007/s42241-018-0002-0.

Ely, J.S., Evans, D.K., 2010. Plant communities of selected embayments along the mid- to mid-upper ohio river floodplain. J Bot Res Inst Tex 4, 411–433.

Engelen, L., de Mulder, T., 2020. Application of 3D-PTV to mass exchange in an open-channel flow past a lateral embayment. Meas Sci Technol 31. https://doi.org/10.1088/1361-6501/ab6672.

Engelen, L., Perrot-Minot, C., Mignot, E., Rivière, N., de Mulder, T., 2020. Experimental study of bidirectional seiching in an open-channel, lateral cavity in the time and frequency domain. Phys Rev Fluids 5, 1–20. https://doi.org/10.1103/PhysRevFluids.5.104801.

Engelen, L., Perrot-Minot, C., Mignot, E., Rivière, N., de Mulder, T., 2021. Lagrangian study of the particle transport past a lateral, open-channel cavity. Phys. Fluids 33. https://doi.org/10.1063/5.0030922.

Engelhardt, C., Krüger, A., Sukhodolov, A., Nicklisch, A., 2004. A study of phytoplankton spatial distributions, flow structure and characteristics of mixing in a river reach with groynes. J Plankton Res 26, 1351–1366. https://doi.org/10.1093/plankt/fbh125.

Gualtieri, C., Jiménez, L., & Rodríguez, J. (2010, May). Modelling turbulence and solute transport in a square dead zone. In *1st European IAHR Congress, Edinburgh (Gran Bretagna). May* (Vol. 4, No. 6).

Gualtieri, C., 2008. Numerical simulation of flow patterns and mass exchange processes in dead zones. Proc. iEMSs 4th Biennial Meeting - Int. Congress on Environmental Modelling and Software: Integrating Sciences and Information Technology for Environmental Assessment and Decision Making, iEMSs 2008 1, 150–161.

Harvey, J.W., 2016. Hydrologic Exchange Flows and Their Ecological Consequences in River Corridors. In: Jones, J.B., Stanley, E.H. (Eds.), Stream Ecosystems in a Changing Environment. Academic Press, Boston, pp. 1–83. https://doi.org/10.1016/B978-0-12-405890-3.00001-4.

Harvey, J., Gooseff, M., 2015. River corridor science: Hydrologic exchange and ecological consequences from bedforms to basins. Water Resour Res 51, 6893–6922. https://doi.org/10.1002/2015WR017617.

Jackson, T.R., Haggerty, R., Apte, S.v., 2013. A fluid-mechanics based classification scheme for surface transient storage in riverine environments: Quantitatively separating surface from hyporheic transient storage. Hydrol Earth Syst Sci 17, 2747–2779. https://doi.org/10.5194/hess-17-2747-2013.

Jackson, T.R., Apte, S.v., Haggerty, R., Budwig, R., 2015. Flow structure and mean residence times of lateral cavities in open channel flows: influence of bed roughness and shape. Environ. Fluid Mech. 15, 1069–1100. https://doi.org/10.1007/s10652-015-9407-2.

Jones, R.C., 2020. Recovery of a Tidal Freshwater Embayment from Eutrophication: a Multidecadal Study. Estuar. Coasts 43, 1318–1334. https://doi.org/10.1007/s12237-020-00730-3.

Juez, C., Bühlmann, I., Maechler, G., Schleiss, A.J., Franca, M.J., 2018a. Transport of suspended sediments under the influence of bank macro-roughness. Earth Surf Process Landf 43, 271–284. https://doi.org/10.1002/esp.4243.

Juez, C., Thalmann, M., Schleiss, A.J., Franca, M.J., 2018b. Morphological resilience to flow fluctuations of fine sediment deposits in bank lateral cavities. Adv Water Resour 115, 44–59. https://doi.org/10.1016/j.advwatres.2018.03.004.

Kara, S., Kara, M.C., Stoesser, T., Sturm, T.W., 2015. Free-Surface versus Rigid-Lid LES Computations for Bridge-Abutment Flow. J. Hydraul. Eng. 141, 04015019. https://doi.org/10.1061/(asce)hy.1943-7900.0001028.

Khosronejad, A., Arabi, M.G., Angelidis, D., Bagherizadeh, E., Flora, K., Farhadzadeh, A., 2020. A comparative study of rigid-lid and level-set methods for LES of open-channel flows: morphodynamics. Environ Fluid Mech 20, 145–164. https://doi.org/10.1007/s10652-019-09703-y.

Kim, H.S., Kimura, I., Shimizu, Y., 2015. Bed morphological changes around a finite patch of vegetation. Earth Surf Process Landf 40, 375–388. https://doi.org/10.1002/esp.3639.

King, A.T., Tinoco, R.O., Cowen, E.A., 2012. A k-ε turbulence model based on the scales of vertical shear and stem wakes valid for emergent and submerged vegetated flows. J Fluid Mech 701, 1–39. https://doi.org/10.1017/jfm.2012.113.

Kozerski, H.P., Schwartz, R., Hintze, T., 2006. Tracer measurements in groyne fields for the quantification of mean hydraulic residence times and of the exchange with the stream. Acta Hydroch. Hydrob. 34, 188–200. https://doi.org/10.1002/aheh.200400629.

Kraus, R.T., Jones, R.C., 2012. Fish abundances in shoreline habitats and submerged aquatic vegetation in a tidal freshwater embayment of the Potomac River. Environ Monit Assess 184, 3341–3357. https://doi.org/10.1007/s10661-011-2192-6.

Kurzke, M., Weitbrecht, V., Jirka, G.H., 2002. Laboratory concentration measurements for determination of mass exchange between groin fields and main stream, in: In: Proceedings. River Flow 2002, Louvain-La-Neuve, Belgium 2002.

Lu, J., Dai, H.C., 2016. Large eddy simulation of flow and mass exchange in an embayment with or without vegetation. Appl Math Model 40, 7751–7767. https://doi.org/10.1016/j.apm.2016.03.026.

Maceina, M.J., Slipke, J.W., Grizzle, J.M., 1999. Effectiveness of Three Barrier Types for Confining Grass Carp in Embayments of Lake Seminole, Georgia. N Am J Fish Manag 19, 968–976. https://doi.org/10.1577/1548-8675(1999)019<0968:eotbtf>2.0.co;2.

McCoy, A., Constantinescu, G., Weber, L., 2007. A numerical investigation of coherent structures and mass exchange processes in channel flow with two lateral submerged groynes. Water Resour Res 43, 1–26. https://doi.org/10.1029/2006WR005267.

Meile, T., Boillat, J.-L., Schleiss, A.J., 2010. Unsteady flow in a channel with large scale bank roughness. River Flow 2010, 621–630.

Meile, T., Boillat, J.-L., Schleiss, A.J., 2011. Flow Resistance Caused by Large-Scale Bank Roughness in a Channel. J. Hydraul. Eng. 137, 1588–1597. https://doi.org/10.1061/(ASCE)HY.1943-7900.0000469.

Mignot, E., Brevis, W., 2020. Coherent Turbulent Structures within Open-Channel Lateral Cavities. J. Hydraul. Eng. 146, 1–8. https://doi.org/10.1061/(ASCE)HY.1943-7900.0001698.

Mignot, E., Cai, W., Launay, G., Riviere, N., Escauriaza, C., 2016. Coherent turbulent structures at the mixing-interface of a square open-channel lateral cavity. Phys. Fluids 28. https://doi.org/10.1063/1.4945264.

Mignot, E., Cai, W., Polanco, J.I., Escauriaza, C., Riviere, N., 2017. Measurement of mass exchange processes and coefficients in a simplified open-channel lateral cavity connected to a main stream. Environ. Fluid Mech. 17, 429–448.

Mignot, E., Cai, W., Riviere, N., 2019. Analysis of the transitions between flow patterns in open-channel lateral cavities with increasing aspect ratio. Environ. Fluid Mech. 19, 231–253. https://doi.org/10.1007/s10652-018-9620-x.

Nepf, H.M., 2012a. Flow and Transport in Regions with Aquatic Vegetation. Annu Rev Fluid Mech 44, 123–142. https://doi.org/10.1146/annurev-fluid-120710-101048.

Nepf, H.M., 2012b. Hydrodynamics of vegetated channels. J. Hydraul. Res. 50, 262–279. https://doi.org/10.1080/00221686.2012.696559.

Nicoud, F., Ducros, F., 1999. Subgrid-scale stress modelling based on the square of the velocity gradient tensor. Flow Turbul Combust 62, 183–200. https://doi.org/10.1023/A:1009995426001.

Oldham, C.E., Sturman, J.J., 2001. The effect of emergent vegetation on convective flushing in shallow wetlands: Scaling and experiments. Limnol Oceanogr 46, 1486–1493. https://doi.org/10.4319/lo.2001.46.6.1486.

Olesen, B., 1996. Regulation of light attenuation and eelgrass Zostera marina depth distribution in a Danish embayment. Mar Ecol Prog Ser 134, 187–194. https://doi.org/10.3354/meps134187.

Oliveira, L., Queiroz, F., Yamasaki, T., Janzen, J., Gualtieri, C., 2021. Effects of the Turbulent Schmidt Number on the Mass Exchange of a Vegetated Lateral Cavity, in: EGU General Assembly 2021. https://doi.org/10.5194/egusphere-egu21-5708.

Ouro, P., Fraga, B., Viti, N., Angeloudis, A., Stoesser, T., Gualtieri, C., 2018. Instantaneous transport of a passive scalar in a turbulent separated flow. Environ. Fluid Mech. 18, 487–513. https://doi.org/10.1007/s10652-017-9567-3.

Ouro, P., Juez, C., Franca, M., 2020. Drivers for mass and momentum exchange between the main channel and river bank lateral cavities. Adv Water Resour 137. https://doi.org/10.1016/j.advwatres.2020.103511.

Perrot-Minot, C., Mignot, E., Perkins, R., Lopez, D., Riviere, N., 2020. Vortex shedding frequency in open-channel lateral cavity. J Fluid Mech 892. https://doi.org/10.1017/jfm.2020.186.

Poletto, R., Craft, T., Revell, A., 2013. A new divergence free synthetic eddy method for the reproduction of inlet flow conditions for les. Flow Turbul Combust 91, 519–539. https://doi.org/10.1007/s10494-013-9488-2.

Reynolds, C.S., Carling, P., Beven, K., 1991. Flow in river channels: new insights into hydraulic retention. Arch. Hydrobiol 121, 171–179.

Ribi, J.-M., Boillat, J.-L., Peter, A., Schleiss, A.J., 2014. Attractiveness of a lateral shelter in a channel as a refuge for juvenile brown trout during hydropeaking. Aquat Sci 76, 527–541. https://doi.org/10.1007/s00027-014-0351-x.

Rodi, W., Constantinescu, G., Stoesser, T., 2013. Large-Eddy Simulation in Hydraulics, 1st ed. CRC Press/Balkema, Leiden.

Sandoval, J., Mignot, E., Mao, L., Pastén, P., Bolster, D., Escauriaza, C., 2019. Field and Numerical Investigation of Transport Mechanisms in a Surface Storage Zone. J Geophys Res Earth Surf 124, 938–959. https://doi.org/10.1029/2018JF004716.

Sanjou, M., Nezu, I., 2013. Hydrodynamic characteristics and related mass-transfer properties in open channel flows with rectangular embayment zone. Environ Fluid Mech 13 (6), 527–555.

Sanjou, M., Okamoto, T., Nezu, I., 2018. Dissolved oxygen transfer into a square embayment connected to an open-channel flow. Int J Heat Mass Transf 125, 1169–1180. https://doi.org/10.1016/j.ijheatmasstransfer.2018.04.107.

Staentzel, C., Combroux, I., Barillier, A., Grac, C., Chanez, E., Beisel, J.N., 2019. Effects of a river restoration project along the Old Rhine River (France-Germany): Response of macroinvertebrate communities. Ecol Eng 127, 114–124. https://doi.org/10.1016/j.ecoleng.2018.10.024.

Sukhodolov, A.N., Sukhodolova, T.A., Krick, J., 2017. Effects of vegetation on turbulent flow structure in groyne fields. J. Hydraul. Res. 55, 1–15. https://doi.org/10.1080/00221686.2016.1211183.

Sukhodolov, A., Uijttewaal, W.S.J., Engelhardt, C., 2002. On the correspondence between morphological and hydrodynamical patterns of groyne fields. Earth Surf Process Landf 27, 289–305. https://doi.org/10.1002/esp.319.

Tuna, B.A., Tinar, E., Rockwell, D., 2013. Shallow flow past a cavity: Globally coupled oscillations as a function of depth. Exp Fluids 54. https://doi.org/10.1007/s00348-013-1586-3.

Uijttewaal, B.W.S.J., Lehmann, D., Van Mazijk, A., 2001. Exchange Processes Between a River and Model Experiments Its Groyne Fields : Model Experiments. J. Hydraul. Eng. 127, 928–936.

Valyrakis, M., Liu, D., Turker, U., Yagci, O., 2021. The role of increasing riverbank vegetation density on flow dynamics across an asymmetrical channel. Environ Fluid Mech 21, 643–666. https://doi.org/10.1007/s10652-021-09791-9.

Vandenbruwaene, W., Temmerman, S., Bouma, T.J., Klaassen, P.C., de Vries, M.B., Callaghan, D.P., van Steeg, P., Dekker, F., van Duren, L.A., Martini, E., Balke, T., Biermans, G., Schoelynck, J., Meire, P., 2011. Flow interaction with dynamic vegetation patches: Implications for biogeomorphic evolution of a tidal landscape. J Geophys Res Earth Surf 116, n/a-n/a. https://doi.org/10.1029/2010JF001788.

Vargas-Luna, A., Crosato, A., Uijttewaal, W.S.J., 2015. Effects of vegetation on flow and sediment transport: Comparative analyses and validation of predicting models. Earth Surf Process Landf 40, 157–176. https://doi.org/10.1002/esp.3633.

Ward, L.G., Michael Kemp, W., Boynton, W.R., 1984. The influence of waves and seagrass communities on suspended particulates in an estuarine embayment. Mar Geol 59, 85–103. https://doi.org/10.1016/0025-3227(84)90089-6.

Watanabe, K., Nagy, H.M., Noguchi, H., 2002. Flow structure and bed-load transport in vegetation flow. Advances in Hydraulics and Water Engineering. 214–218. https://doi.org/10.1142/9789812776969_0036.

Watts, R.J., Johnson, M.S., 2004. Estuaries, lagoons and enclosed embayments: Habitats that enhance population subdivision of inshore fishes. Mar Freshw Res 55, 641–651. https://doi.org/10.1071/MF04051.

Weitbrecht, V., 2004. Influence of Dead-Water Zones on the Dispersive Mass Transport in Rivers. In: Dissertationsreihe Am Institut Für Hydromechanik Der Universität Karlsruhe (TH). Karlsruhe Institute of Technology, Karlsruhe. https://doi.org/10.5445/KSP/1242004.

Weitbrecht, V., Socolofsky, S.a., Jirka, G.H., 2008. Experiments on Mass Exchange between Groin Fields and Main Stream in Rivers. J. Hydraul. Eng. 134, 173–183. https://doi.org/10.1061/(ASCE)0733-9429(2008)134:2(173).

Xavier, M.L.M., Janzen, J.G., Nepf, H., 2018. Numerical modeling study to compare the nutrient removal potential of different floating treatment island configurations in a stormwater pond. Ecol Eng 111, 78–84. https://doi.org/10.1016/j.ecoleng.2017.11.022.

Xiang, K., Yang, Z., Huai, W., Ding, R., 2019. Large eddy simulation of turbulent flow structure in a rectangular embayment zone with different population densities of vegetation. Environ. Sci. Pollut. Res. 26, 14583–14597. https://doi.org/10.1007/s11356-019-04709-x.

Xiang, K., Yang, Z., Wu, S., Gao, W., Li, D., Li, Q., 2020. Flow hydrodynamics of the mixing layer in consecutive vegetated groyne fields. Phys. Fluids 32, 1–22. https://doi.org/10.1063/5.0006317.

Yamasaki, T.N., de Lima, P.H.S., Silva, D.F., de Preza A., C.G., Janzen, J.G., Nepf, H.M., 2019. From patch to channel scale: The evolution of emergent vegetation in a channel. Adv Water Resour. https://doi.org/10.1016/j.advwatres.2019.05.009.

Yamasaki, T.N., Walker, C., Janzen, J.G., Nepf, H., 2022. Flow distribution and mass removal in floating treatment wetlands arranged in series and spanning the channel width. Journal of Hydro-environment Research 44, 1–11. https://doi.org/10.1016/j.jher.2022.07.001.

Zhang, Y., Lai, X., Ma, J., Zhang, Q., Yu, R., Yao, X., Deng, H., 2021. Field study on flow structures within aquatic vegetation under combined currents and small-scale waves. Hydrol Process 35. https://doi.org/10.1002/hyp.14121.

Zhiyin, Y., 2015. Large-eddy simulation: Past, present and the future. Chin. J. Aeronaut. 28, 11–24. https://doi.org/10.1016/j.cja.2014.12.007.